

**A regional real-time
forecast of marine
boundary layers
during VOCALS-Rex**

S. Wang et al.

A regional real-time forecast of marine boundary layers during VOCALS-Rex

S. Wang¹, L. W. O'Neill², Q. Jiang³, S. P. de Szoeke⁴, X. Hong¹, H. Jin¹,
W. T. Thompson¹, and X. Zheng⁵

¹Naval Research Laboratory, Monterey, CA, USA

²National Research Council, Naval Research Laboratory, Monterey, CA, USA

³University Corporation for Atmospheric Research, Monterey, CA, USA

⁴Oregon State University, College of Ocean and Atmospheric Sciences, Corvallis, Oregon, USA

⁵RSMA, University of Miami, Miami, FL, USA

Received: 7 July 2010 – Accepted: 7 July 2010 – Published: 4 August 2010

Correspondence to: S. Wang (shouping.wang@nrlmry.navy.mil)

Published by Copernicus Publications on behalf of the European Geosciences Union.

Title Page

Abstract

Introduction

Conclusions

References

Tables

Figures

⏪

⏩

◀

▶

Back

Close

Full Screen / Esc

Printer-friendly Version

Interactive Discussion

Abstract

This paper presents an evaluation and validation of the Naval Research Laboratory's COAMPS real-time forecasts during the VOCALS-Rex over the area off the west coast of Chile/Peru in the Southeast Pacific during October and November 2008. The analyses focus on the marine boundary layer (MBL) structure. These forecasts are compared with lower troposphere soundings, surface measurements, and satellite observations. The predicted mean MBL cloud and surface wind spatial distributions are in good agreement with the satellite observations. The large-scale longitudinal variation of the MBL structure along 20° S is captured by the forecasts. That is, the MBL heights increase toward the open ocean, the moisture just above the inversion decreases, and the MBL structure becomes more decoupled offshore. The observed strong wind shear across the cloud-top inversion in coastal area at 20° S was correctly predicted by the model. Our results show that the sporadic cloud spatial and temporal distribution in the 15 km grid mesh is caused by grid-scale convection likely due to a lack of a shallow cumulus convection parameterization in the model. Both observations and model forecasts show wind speed maxima near the top of MBL along 20° S, which is consistent with the west-ward upslope of the MBL heights based on the thermal wind relationship. The forecasts produced well-defined diurnal variations in the spatially averaged MBL structure, although the overall signal is weaker than those derived from the in situ measurements and satellite data. The MBL heights are generally underpredicted in the nearshore area. The analysis of the sensitivity simulations with regard to grid resolution suggests that the under-prediction is likely associated with over-prediction of the mesoscale downward motion and cold advection along the coast.

1 Introduction

The marine boundary layer is known to play key roles in regulating large- and meso-scale atmospheric circulations as it serves as the major source of moist available en-

ACPD

10, 18419–18466, 2010

A regional real-time forecast of marine boundary layers during VOCALS-Rex

S. Wang et al.

Title Page

Abstract

Introduction

Conclusions

References

Tables

Figures

⏪

⏩

◀

▶

Back

Close

Full Screen / Esc

Printer-friendly Version

Interactive Discussion



ergy for atmospheric circulation and the major sink of atmospheric kinetic energy (e.g., Lorenz, 1978; Palmen and Newton, 1969). Clouds are frequently present within the MBL in the form of overcast stratocumulus/stratus, organized scattered shallow cumulus clouds or transitional mixture of both; they cover a third of the world's oceans and form a persistent feature of the earth climate and regional weather (Klein and Hartmann, 1993; Felsch and Whitlatch, 1993). These clouds have a significant influence on the underlying surface energy budget by significantly reflecting incoming solar energy, but only moderately increasing downward longwave radiative flux (Klein and Hartmann, 1993). In addition, the cloud-top radiative cooling created by the clouds and the latent heat released by the convective updrafts fundamentally change the nature of the turbulence dynamics compared to a cloud-free MBL, leading to changes in thermodynamic and wind profiles in the MBL (Lilly, 1968). Consequently, air-sea interaction processes are profoundly impacted by the presence of these clouds at both global and regional scales. It is of great importance, therefore, that coupled climate and mesoscale models are able to realistically predict the MBL structure, cloud coverage and their variability (Ma et al., 1996; Bony and Dufresne, 2005; de Szoeke et al., 2006, and Shulman et al., 2007).

The cloud-topped MBL is, however, notoriously difficult to simulate, because turbulence-cloud interaction processes cannot be explicitly resolved at current grid resolutions of global and regional models; and thus they must be parameterized. For example, an interactive turbulence-shallow convection parameterization is essential to predict the transition from stratocumulus to shallow cumulus clouds (Park and Bretherton, 2009). Furthermore, mesoscale cloud variability may also be driven by the so-called aerosol-cloud-precipitation interaction mechanism proposed by Albrecht (1989), in which low CCN (Cloud Condensation Nuclei) concentration promotes more precipitation, leading to the destruction and structural change of the clouds (e.g., Stevens et al., 2005; Wang and Feingold, 2009). The representation of this complex interaction process has not yet been developed for use in regional and global models.

Two primary focuses of VOCALS-Rex (Variability of the American Monsoons

A regional real-time forecast of marine boundary layers during VOCALS-Rex

S. Wang et al.

Title Page

Abstract

Introduction

Conclusions

References

Tables

Figures



Back

Close

Full Screen / Esc

Printer-friendly Version

Interactive Discussion



A regional real-time forecast of marine boundary layers during VOCALS-Rex

S. Wang et al.

Title Page

Abstract

Introduction

Conclusions

References

Tables

Figures



Back

Close

Full Screen / Esc

Printer-friendly Version

Interactive Discussion



Ocean-Cloud-Atmosphere-Land Study-Regional experiment) are: 1) the aerosol-cloud-precipitation interaction in the MBL; and 2) chemical and physical couplings between the upper ocean, the land, and the atmosphere (Woods et al., 2006). The field campaign took place off the west coast of Chile/Peru in the Southeast Pacific during October and November 2008. Comprehensive measurements were made on many platforms including aircrafts, ships, satellites, buoys, and land based observation sites to provide description of the MBL structure, turbulence dynamics, aerosol-cloud microphysics and air–sea interaction. Particularly, intensive observations were carried out along the latitude 20° S to provide detailed time-height and longitude-height cross-sections of the MBL.

One important motivation for VOCALS-Rex is to improve the prediction of MBL clouds by both global and regional models. Because of the prominent impacts of MBL clouds on global climate as discussed earlier, modeling efforts have traditionally emphasized global models. In the last few decades, however, an increasing number of studies has focused on the regional modeling investigations of MBL clouds, including regional simulations using a simple two-layer model (Wang et al., 1994), cloud evaluation and process studies using mesoscale models in a regional climate mode (e.g., Wang et al., 2004a and b; McCaa and Bretherton, 2003; Garreaud and Muñoz, 2004), investigations of cloud and dynamic processes in case studies (Mocko and Cotton, 1995; Mechem and Kogan, 2003; Thompson et al., 2005), and study of shallow cumulus effects in regional ocean-atmosphere coupled climate model (de Szoeke et al., 2006). These regional model studies demonstrate that the fidelity of the MBL cloud simulations is highly dependent on the quality of the cloud and turbulence parameterizations as well as the accuracy of the large- and mesoscale flows. A recent assessment of current global and regional models clearly shows weakness in the simulated cloudiness and MBL heights, two important parameters in the MBL cloud prediction (Wyant et al., 2010).

During October–November 2008, NRL's (Naval Research Laboratory's) COAMPS® (Coupled Ocean/Atmosphere Mesoscale Prediction System) real-time forecasts were

performed in support of VOCALS-Rex. The current work presented here focuses on evaluation and validation of these MBL forecasts using observations taken during the VOCALS-Rex field program. It is motivated by the following questions: to what degree do the predicted cloud fields such as integrated cloud water path agree with observations? To what degree does the predicted MBL structure agree with that observed? What specific aspects of the model can be improved to better simulate the MBL cloud system?

Section 2 describes COAMPS, the forecast setup, and the observational datasets. Sections 3–6 analyze COAMPS regional fields, MBL variations along 20° S, statistics of the surface variables, and mean MBL diurnal structure. Section 7 discusses the issue the model grid resolution and Sect. 8 gives the summary and conclusion.

2 COAMPS-real-time forecast setup and observation datasets

The atmospheric component of COAMPS[®] represents both a forecast model and a complete three-dimensional data assimilation system. The forecast model is a finite-difference approximation to the fully incompressible and non-hydrostatic equations that govern atmospheric motions (Hodur, 1997). The main model physical representations relevant to this study are briefly described as follows. For the boundary layer prediction, the surface layer is represented using the modified version of the Louis (1982) surface flux parameterization as formulated by Wang et al. (2002); turbulence mixing processes are parameterized following the Mellor-Yamada's level-1.5 turbulence closure model that predicts turbulence kinetic energy and determines the turbulent fluxes in terms of the down-gradient transport approach (Mellor and Yamada, 1982). To account for latent heat effect of clouds on the buoyancy in turbulence mixing, the subgrid-scale cloud fraction is calculated using a Gaussian distribution of turbulent fluctuations of conserved variables as discussed in Sommeria and Deardoff (1977), Melor (1977), and Burk and Thompson (1989). The cumulus parameterization of Kain and Fritsch (1990) is used to represent the convection at the subgrid scale; and it is only acti-

A regional real-time forecast of marine boundary layers during VOCALS-Rex

S. Wang et al.

Title Page

Abstract

Introduction

Conclusions

References

Tables

Figures



Back

Close

Full Screen / Esc

Printer-friendly Version

Interactive Discussion



A regional real-time forecast of marine boundary layers during VOCALS-Rex

S. Wang et al.

Title Page

Abstract

Introduction

Conclusions

References

Tables

Figures



Back

Close

Full Screen / Esc

Printer-friendly Version

Interactive Discussion



vated when the grid size is greater than 10 km. The current version of this convection scheme, however, is not designed to represent shallow cumulus clouds, which is a limitation that will be discussed further in Sect. 4. Clouds and precipitation at grid scale are predicted using the single moment scheme of cloud microphysics formulated by Rutledge and Hobbs (1983). Recently, the four-stream radiation parameterization of Fu and Liou (1992) has been implemented in COAMPS (Liu et al., 2009).

The initialization of COAMPS forecasts is performed by a data assimilation system that uses multivariate optimum interpolation analyses of soundings, surface and satellite data and blended with the previous 12-h COAMPS forecasted fields. Lateral boundary conditions for the outermost domain are provided by the Navy Operational Global Analysis and Prediction System (NOGAPS) forecast fields. The sea surface temperature (SST) is generated by the NRL Coupled Ocean Data Assimilation System (NCODA), which applies a three-dimensional, multivariate, optimum-interpolation method and integrates all available ocean observations in real time, including ship, buoy, and satellite observations as discussed in Cummings (2005).

During VOCALS-Rex, COAMPS provided 48 h twice-daily forecasts with a 3-h interval output, initialized at 00:00 UTC and 12:00 UTC, between 20 October and 29 November 2008. As shown in Fig. 1, the forecast domain is configured to contain three nested grid meshes (45 km, 15 km, and 5 km) with 45 levels in the vertical, of which 26 levels reside below 2.5 km. Our analysis is focused on the forecast from the 15 km domain, as this grid mesh covers most of the VOCALS-Rex observation areas and has a relatively high horizontal resolution. Some results from the 45 km and 5 km grid meshes will also be presented in this analysis to provide comparisons.

The observational data employed in this study include both satellite observations and in-situ measurements made during VOCALS-Rex. Satellite observations of liquid water path (LWP) and surface wind speed are from 4 passive microwave radiometers onboard the AMSR-E (Advanced Microwave Scanning Radiometer – Earth Observing System), TRMM (Tropical Rainfall Measurement Mission) Microwave Imager, and the SSM/I (Special Sensor Microwave Imager) F13 and F15 satellites. Satellite SST

A regional real-time forecast of marine boundary layers during VOCALS-Rex

S. Wang et al.

[Title Page](#)[Abstract](#)[Introduction](#)[Conclusions](#)[References](#)[Tables](#)[Figures](#)[⏪](#)[⏩](#)[◀](#)[▶](#)[Back](#)[Close](#)[Full Screen / Esc](#)[Printer-friendly Version](#)[Interactive Discussion](#)

fields from the AMSR-E and TMI satellites were used as an independent evaluation of the NCODA SST fields used as the lower boundary condition in these COAMPS forecasts. Additionally, vector surface winds from QuickSCAT (Quick Scatterometer) are also used for comparison. Atmospheric sounding data used in this work were collected on board NOAA R/V Ronald H. Brown (RHB) along 20° S and on board CIR-PAS (Center for Interdisciplinary Remotely Piloted Aircraft Studies) Twin Otter research flights at the location of 20° S and 72° W. Ship-based surface observations and rawinsondes are available every 10 min from the multi-year NOAA tropical eastern Pacific 10-min synthesis data set from the VOCALS-Rex RHB cruise and data collected at the WHOI buoy located at 85° W and 20° S. Readers are referred to the VOCALS website (<http://catalog.eol.ucar.edu/vocals/>) for a complete description of the observations and the platforms.

3 Regional fields

We first examine the large-scale features by comparing the COAMPS 41-day (20 October to 29 November) averaged SST and wind fields on the 45 km grid mesh with those derived from the satellite data as shown in Fig. 2. The model SST accurately captures all the major features shown by the AMSR-E and TMI SST field. Both SST fields are colder close to the Chilean coast (Fig. 2a and b), driven by the low-level jet of strong southerly winds parallel to the coast shown in the wind fields between 40° S and 25° S (Fig. 2c and d). The local warm SST area centered at 72° W and 20° S results from the weak southerly winds blocked by the Andes. A broad region of cold SST (green shaded) is present to the northwest of the coastal upwelling zone; it appears to result from the oceanic cold advection driven by the southeast wind from the low-level jet area to the northern side of the high pressure system. Even though the model SST is a product of the ocean data assimilation system, the AMSR-E and TMI data were not included in NCODA for the ocean analysis. Therefore, this comparison also serves as

an independent validation of the NCODA product.

The forecasted surface wind vectors agree with the satellite QuickSCAT data in the following main features. The southerly coastal jet along the Chilean coast is consistent with the satellite winds in the overall correct location and direction of the jet axis, although the simulated jet appears stronger and extend further north. Weak wind speed areas are present near the subtropical high pressure center at 105° W and 31° S and nearshore at 20° S; and the relatively high wind speeds exist in the northern side of the high pressure system (Fig. 2e). The Chilean low-level jet often takes place in the austral spring and summer seasons and appears to be associated with the northerly directed pressure gradient force along the coast induced by mid-latitude synoptic conditions (Garreaud and Muñoz, 2005; Muñoz and Garreaud, 2005). A recent study by Jiang et al. (2010) using the COAMPS forecasts identifies that the subtropical high pressure system is a major forcing regulating the low-level jet variability. Readers are referred to these papers for comprehensive discussions on the issues of the Chilean low-level jet.

As shown in Fig. 2f, the main features of the predicted winds just above the MBL inversion at 1.8 km height include the anti-cyclonic circulation associated with the subtropical high pressure system and the weak wind speed area between the high pressure system and the coast. In particular, a narrow northerly jet flow extends from 15° S to 30° S along the coast, contrasting the southerly flow within the MBL (Fig. 2d) and resulting in a sharp wind shear across the inversion. The existence of the strong wind shear is confirmed by the aircraft observations as will be presented later.

We next examine the cloud and wind fields with a focus on the VOCALS-Rex area using the 15 km grid forecasts. The satellite data used for this comparison are derived from the microwave measurements taken on AMSR-E, SSMI and TMI satellites, which together have a sampling frequency of 4–8 times daily at each grid point in the domain, which depend on detailed sampling characteristics of each satellite.

Figure 3a and b show that the general patterns of the mean liquid water path (LWP) fields from the forecast and satellite data are very similar. Both LWP fields are char-

A regional real-time forecast of marine boundary layers during VOCALS-Rex

S. Wang et al.

Title Page

Abstract

Introduction

Conclusions

References

Tables

Figures



Back

Close

Full Screen / Esc

Printer-friendly Version

Interactive Discussion



A regional real-time forecast of marine boundary layers during VOCALS-Rex

S. Wang et al.

Title Page

Abstract

Introduction

Conclusions

References

Tables

Figures



Back

Close

Full Screen / Esc

Printer-friendly Version

Interactive Discussion



acterized by extensive coverage over the southeast Pacific with relatively thick LWP (~ 100 to 120 g m^{-2}) covering the western part of the domain and thinner clouds along the coast. The LWP decreases significantly to the south of 25° S , where subsidence tends to dominate near the center of the high pressure system. The COAMPS under-
 5 predicts nearshore clouds, particularly along the coast between 16° S and 20° S and to the south of 25° S . This deficiency is likely caused by MBL heights that are too low compared with those observed as discussed in the next sections.

As shown in Fig. 3c and d, surface wind speeds from both the COAMPS simulations and the satellite data indicate a weak wind area near the coast between 25° S and
 10 17° S . Both tend to have maximum values in the low-level jet region off the coast of Chile and to the south of 25° S , although the maxima from the forecast ($\sim 8 \text{ m s}^{-1}$) are stronger than those from the satellite observations ($\sim 7 \text{ m s}^{-1}$). The center of the Southeast Pacific high pressure systems is characterized by weak winds and low LWP values associated with strong subsidence, as shown in both the modeled results and
 15 satellite observations. The comparison for the 15 km mesh is generally consistent with that for the 45 km mesh.

Diurnal variability in the cloud field is a dominant feature over the southeast Pacific (e.g., Rozendaal et al., 1995; O'Dell et al., 2008; Wood et al., 2009). To examine the statistical behavior of diurnal variation of the clouds and wind speeds, a harmonic
 20 regression analysis with the diurnal cycle is performed on both the forecasts and the satellite data (Figs. 4 and 5). Because sampling rate of the satellite data is about 4–5 times per day, we only focus on the dominant 24 h diurnal cycle. The statistical diurnal amplitude of liquid water path (LWP) derived from both the forecasts and satellite have similar maximum values of 70 g m^{-2} , which is about half of the maximum mean values
 25 (130 g m^{-2}), implying presence of a significant cloud diurnal variation. The diurnal variation is primarily driven by the cloud solar absorption during daytime, which tends to stabilize the MBL and decouple the cloud from the surface-based subcloud layer (Nicholls, 1984; Turton and Nicholls, 1987). Significant differences are evident between the diurnal amplitude derived from the satellite and that from the forecasts. The satellite

field is relatively smooth and continuous, while the forecast is spotty and discontinuous. Further examination of the instantaneous cloud fields reveals that this discontinuity occurs probably due to the lack of shallow cumulus convection parameterization in the model, which will be discussed further in the next section.

To estimate the diurnal contribution to the total LWP variability, we calculate the correlation of the LWP diurnal harmonic regression with the satellite and the forecasts, respectively. The correlation values for the COAMPS (~ 0.3 – 0.5) are smaller than those for the satellite data (~ 0.6 – 0.8) over large areas to the west of 72° W and the north of 25° S. These values indicate that while the diurnal cycle can only account for 10–25% of the total variance in the predicted LWP, it accounts for as high as 36–60% in the satellite data over these areas. Over the coastal areas near 20° S, the modeled correlation is about 0.6, slightly higher than the observation. The phase of the diurnal variation in the forecasts is consistent with the satellite data (Fig. 4e and f), as both results show the maxima occurring between midnight and 08:00 a.m. LST.

Surface wind speeds from both the forecast and the satellite data show diurnal signals over large areas off the Chilean coast reaching as far as 82° W as shown in Fig. 5. For the forecast, the area with the largest diurnal amplitude (~ 1.2 – 1.8 m s $^{-1}$) appears to be in regions of relatively weak wind. The western part of the area overlaps the region of the satellite's large amplitudes centered on (80° W, 26° S), whose values (1.2 m s $^{-1}$) are less than the forecasts. Both the forecasts and the satellite place the large diurnal wind speed amplitude areas to the north and northwest of the low-level jet core offshore of central Chile; it is particularly true for model results. This is consistent with Garreaud and Muñoz (2005) who conclude that the diurnal cycle in climatological region of the maximum wind speed is small. This is also consistent with the latitudinal variation of sea-breeze predicted by linear theory (Rotunno, 1983). The correlation pattern of the wind speed and its diurnal variation shows a general agreement between the satellite and the forecasts with larger values covering the coastal area and extending offshore (Fig. 5b and c). For both the COAMPS and satellite wind speed fields, the maximum wind speeds occur in the afternoon along the coast between 25° S and 17° S (Fig. 5e

A regional real-time forecast of marine boundary layers during VOCALS-Rex

S. Wang et al.

Title Page

Abstract

Introduction

Conclusions

References

Tables

Figures



Back

Close

Full Screen / Esc

Printer-friendly Version

Interactive Discussion



and f), which is likely produced by the strengthening of the southerly winds (Rutllant 1993). For other areas, the wind speeds are maximum during the late evening and early morning. The diurnal variation of the surface wind speed only accounts for 10–25% of the variances for the satellite as well as the forecasted results, a percentage much less than that for the clouds.

This regional comparison demonstrates that the predicted mean wind and cloud fields in general agree with the satellite observations, including the low-level jet along the west coast of Chile, the weak wind speed area present near the subtropical high center and in the coastal area near 20° S, the overall LWP distribution pattern, and diurnal phase pattern for both clouds and wind speeds. The predicted diurnal variance of the LWP from COAMPS explains 10–25% of the total variance, a percentage smaller than that (30–60%) derived from the satellite data. Diurnal variation of MBL clouds in the southeast Pacific may also include a 6-h harmonic which is driven by the so-called upsidence wave as discussed by Garreaud and Muñoz (2004) and O’Dell et al. (2008). This variability, however, is not included in the current analysis.

4 20° S MBL cross-section

This section focuses on the evaluation of the COAMPS MBL structure along 20° S using the RHB rawinsondes, NCAR C-130, and CIRPAS Twin-Otter measurements. The RHB had two cruise legs, with first running from 6 October to 3 November and the second from 11 to 29 November. No data were collected 3–10 November between the two periods while it was stationed in Arica, Chile, and only the data collected along 20° S are used here.

Figure 6 compares the time-height cross-section of potential temperature (θ) vertical profiles of the lower atmosphere from the RHB with those from the forecast. This forecasted cross-section is derived using interpolation based on the times and locations of the rawinsondes. The comparison starts at 23:24 UTC 25 October 2008 and ends at 16:00 UTC 28 November 2008, including 196 profiles from each dataset. The ob-

A regional real-time forecast of marine boundary layers during VOCALS-Rex

S. Wang et al.

Title Page

Abstract

Introduction

Conclusions

References

Tables

Figures



Back

Close

Full Screen / Esc

Printer-friendly Version

Interactive Discussion



A regional real-time forecast of marine boundary layers during VOCALS-Rex

S. Wang et al.

Title Page

Abstract

Introduction

Conclusions

References

Tables

Figures

⏪

⏩

◀

▶

Back

Close

Full Screen / Esc

Printer-friendly Version

Interactive Discussion

served nearly well-mixed MBL structure capped by a strong inversion is well predicted. The forecasted jump in θ across the inversion appears to be comparable to what was observed, although the modeled inversion layer thickness is larger, probably due to the limited vertical resolution in the model. The modeled MBL height (z_i) was at 1.2 km at the start on 25 October, reached a maximum of 2 km at 85.8° W on the same day, and then gradually lowered to 600 m nearshore at 71° W and 18.5° S on 3 November. For the first 9 days, the variation of the forecasted z_i closely followed that from the observations except that the RHB z_i stays above 1 km near the coast. At the start of leg 2, the z_i was again low at 600 m, and then immediately increased to 1.4 km and varied little afterwards. In contrast, the RHB z_i stayed at ~ 1.3 km until 18 November, after which time it changed considerably and reached a maximum of 2 km. In general, the model captures the observed MBL z_i very well for the first leg of the RHB, but lack the variability comparable to the RHB observations in leg 2. The modeled z_i is generally lower than in the RHB observations, particularly in the nearshore area.

To further examine the MBL vertical structure, we composite the vertical soundings according to their distances to the coast. Figure 7 compares the composite soundings centered at 3 locations: “nearshore” (71.64° W, 19.22° S), “midway” (79.16° W, 19.22° S), and “offshore” (84.5° W, 20.4° S). These composites are produced by averaging the soundings within one degree in longitude of the locations. Most of the forecasted variables closely follow the observations within and above the inversions. The well-mixed θ profiles in the lower MBL are well predicted; the inversion strength also compares well with the observations. There is clear trend of increasing moisture above the inversion toward the coast in both the forecasts and the RHB observations. A weakness in the predicted MBL structure is the lower z_i at both the “nearshore” and “offshore” locations; particularly, z_i is underpredicted nearshore by 450 meters. The model also produced higher moisture just above the inversion and below 2 km, as shown by the specific humidity (q_v) comparison in Fig. 7.

The observed equivalent potential temperature (θ_e) decreases with height below the inversion top (Fig. 7). The negative θ_e gradient becomes stronger toward the open

ocean, suggesting that the MBL tends to be more conditionally unstable offshore, a condition favorable for shallow cumulus development (Stevens, 2007). The model prediction has the similar feature for the “offshore” and “nearshore” locations. Due to the higher values of q_v just above the inversion, the overall change in the modeled θ_e across the MBL is positive at the “midway” location.

Both the model and the RHB observations show wind maxima just below the inversion with diminishing values upward (Fig. 7). The low wind speed above the MBL is associated with the shallowness of a typical subtropical high pressure system. The wind shear across the inversion is consistent with the zonal temperature gradient within the inversion, introduced by the east-west upward slope of the MBL height along 20° S. We can estimate the jump in v across the inversion based on the thermal wind relationship. First, θ should remain the same along the inversion slope. That is,

$$(d\theta)_{z_i} = \left(\frac{\partial\theta}{\partial x}\right)_{z_i} dx + \left(\frac{\partial\theta}{\partial z}\right)_{z_i} dz_i(x) = 0, \quad (1)$$

Using Eq. (1) and the RHB soundings leads to an approximation for the mean zonal temperature gradient within the inversion,

$$\left(\frac{\partial\theta}{\partial x}\right)_{z_i} = -\left(\frac{\partial\theta}{\partial z}\right)_{z_i} \cdot \frac{dz_i}{dx} \sim \frac{13\text{K}}{400\text{m}} \cdot \frac{700\text{m}}{1300 \times 10^3\text{m}} \approx 1.8 \times 10^{-5} \text{K m}^{-1}. \quad (2)$$

The jump in v can then be estimated by the thermal wind relationship

$$\Delta v \sim \frac{g}{f\theta} \cdot \left(\frac{\partial\theta}{\partial x}\right)_{z_i} \Delta z_i \approx \frac{9.8}{-5 \times 10^{-5} \times 300} \cdot 1.8 \times 10^{-5} \cdot 400 \approx -5 \text{ (m s}^{-1}\text{)}, \quad (3)$$

which is close to the observed values -4 to -7 m s^{-1} shown in Fig. 7. Note that this estimate does not depend on Δz_i , which is cancelled out when substituting Eq. (2) in Eq. (3). It is also noticed that the wind shears are weaker from the forecasts than those from the observations at the two offshore locations, while it is stronger nearshore. This is consistent with the fact that z_i was underpredicted both near the coast and at the

A regional real-time forecast of marine boundary layers during VOCALS-Rex

S. Wang et al.

Title Page

Abstract

Introduction

Conclusions

References

Tables

Figures

⏪

⏩

◀

▶

Back

Close

Full Screen / Esc

Printer-friendly Version

Interactive Discussion



Discussion Paper | Discussion Paper | Discussion Paper | Discussion Paper | Discussion Paper

most western locations, resulting in a gentler slope of z_i offshore and a steeper one nearshore.

CIRPAS Twin-Otter research flights provide datasets of coastal MBL structure at the fixed location (20° S, 72° W). Figure 8 compares mean z_i -normalized boundary layer profiles collected from 18 research flights with the model forecasts at the corresponding times. We first note that the mean forecasted MBL height is 751 m, which is about 400 m lower than that derived from the Twin Otter as shown in Fig. 8a, and consistent with the underprediction of z_i found in the nearshore RHB soundings shown in Fig. 7. The mean forecasted temperature and moisture within the MBL in general, agrees well with the Twin Otter observations. Both the model results and Twin Otter observations show apparent wind speed and directional shear across the inversion, although the observed changes are significantly stronger than the forecast. The wind direction changes from southerly within the MBL to northerly just above the inversion in both the observations and model simulations. This wind directional shear is also implied by the narrow band (about 500 km wide) of northerly flow above the MBL as shown in Fig. 2f near 20° S, 72° W. Consequently, this wind shear is associated with the meso- or large-scale dynamics, a key difference from the usual wind shear across the inversion, driven by turbulence mixing. This wind shear may introduce significant turbulence mixing within the entrainment zone, and thus has important implications on the MBL turbulence structure and cloud-top entrainment rate (Wang et al., 2008).

Because the forecasted z_i is considerably lower than the observed z_i , the simulated θ just above the MBL is lower than that of the Twin-Otter observations. The air is also more moist than the observed by 3 g kg^{-1} , further confirming the early result that the air just above the inversion is too moist near the coast in the model compared with the RHB soundings (Fig. 8b). The maximum predicted cloud water (q_c) is only 0.1 g kg^{-1} compared with the observed value, 0.3 g kg^{-1} . The low values of q_c are mainly caused by the lower z_i , which explains the lack of clouds in the forecasts near the coastal area shown in Figs. 3a and 4.

Longitude-height cross-sections of the forecasted 41-day time-averaged MBL struc-

A regional real-time forecast of marine boundary layers during VOCALS-Rex

S. Wang et al.

Title Page

Abstract

Introduction

Conclusions

References

Tables

Figures

◀

▶

◀

▶

Back

Close

Full Screen / Esc

Printer-friendly Version

Interactive Discussion



A regional real-time forecast of marine boundary layers during VOCALS-Rex

S. Wang et al.

Title Page

Abstract

Introduction

Conclusions

References

Tables

Figures

⏪

⏩

◀

▶

Back

Close

Full Screen / Esc

Printer-friendly Version

Interactive Discussion



ture along 20° S are shown in Fig. 9. Also plotted is the MBL height derived from all the NCAR C-130 20° S relative humidity and radar measurements (Bretherton, personal communication). In general, the forecasted z_i increases offshore with increased cloud layer depth. It agrees with the observed z_i reasonably well offshore between 85° W to 75° W, particularly between 78° W and 75° W. The predicted z_i , however, falls sharply near the coast to the east of 75° W, consistent with the comparison with the RHB and Twin-Otter soundings (Figs. 7 and 8.) The average cloud base is higher than the lifting condensation level (LCL). This difference (cloud base level minus LCL) sharply increases from the coast to about 76° W and then increases more gently toward the open ocean, suggesting that the MBL becomes decoupled to the west of 76° W. That is, the MBL thermodynamic profiles depart from being well-mixed and become more stratified due to stronger cloud-top entrainment (Bretherton and Wyant, 1997).

The moisture above the inversion stays constant at about 2 g kg^{-1} offshore (Fig. 9b); it increases significantly to the east of 76° W. This trend agrees with the RHB and NCAR C-130 observations. It has dynamic implications on the MBL turbulence and cloud structure. Since moister air leads to larger downward longwave (LW) radiative flux, the radiative cooling at the cloud top would decrease due to the increase in q_v above the inversion, which would result in lower turbulence intensity in the MBL.

The decoupled feature (Fig. 9a) is also reflected in the TKE longitude-height cross section, which demonstrates that TKE values below clouds considerably decreases to the west of 76° W (Fig. 9c); this suggests that the turbulence is not strong enough to maintain a well-mixed MBL. The overall increase in the MBL height and the more decoupled structure offshore are both consistent with an offshore decrease of lower troposphere stability, as defined by $\Delta\theta = \theta_{3\text{km}} - \theta_{\text{sst}}$ (Fig. 9d) (Bretherton and Wyant, 1997; Klein, 1997). The weak TKE near 78° W is linked to the relatively weak surface buoyancy flux (Fig. 9d) due to the broad cold area in SST extending to 12° S parallel to the coast (green color shaded) shown in Fig. 2a and b.

The 41-day averaged predicted vertical velocity at the inversion height level, presented in Fig. 9d, reaches a minimum ($\sim -0.81 \text{ cm s}^{-1}$) at 72.3° W compared to the

values of -0.3 to -0.4 cm s^{-1} to the west of 75° W . This suggests that the unusually strong subsidence in the model forecasts is likely a main contributor to the thinning of the MBL along the coast. Further analysis will be given in Sect. 7 on the issue of the predicted low MBL heights nearshore.

In Sect. 3, the cloud diurnal amplitude field is shown to be discontinuous and spotty compared to satellite observations (Fig. 4a). Similar spotty cloud fields were also seen in the real-time forecast presentations during VOCALS-Rex daily weather briefings. There is strong evidence that these sporadic cloud fields are likely linked to the so-called grid-scale convection due to the lack of a subgrid-scale shallow cumulus convection parameterization. These sporadic cloud features are more clearly seen in Fig. 10a, which displays a longitude-time cross-section of the predicted LWP along 20° S . Apparent are the appearance of short-lived and relatively thick clouds ($\text{LWP} \sim 500\text{--}700 \text{ g m}^{-2}$) in the background of a well-defined diurnal variation of relatively thin clouds ($\text{LWP} \sim 100\text{--}200 \text{ g m}^{-2}$). Most of these spotty and thick clouds form offshore, where θ_e and q_v in the lower MBL increase westward and decrease with height due to the increase in SST (Figs. 2a and 9b). The decoupled MBL offshore also tends to build up moisture in the subcloud layer by inhibiting upward moisture transport from the subcloud layers. These are favorable conditions for the formation of shallow cumulus clouds. A traditional turbulence closure model like that used in COAMPS (Mellor and Yamada, 1982) is well known to be inappropriate to represent the inhomogeneous turbulence mixing in the cumulus fields with strongly skewed distributions (Siebesma et al., 2007; Golaz et al., 2002). Since there is no shallow cumulus convection parameterization in the model, the instability must then be released by grid-scale convection in the MBL, which leads to the formation of the spotty and relatively thick clouds. A snapshot of these clouds is provided in Fig. 10b, where the grid-scale updrafts of 15 cm s^{-1} produce clouds with 1.5 km in depth and 70 km in width. The overall MBL structure averaged between 90° W and 80° W at this time (Fig. 10c and d) shows a common shallow cumulus thermodynamic structure consisting of a surface-based mixed layer, a thin stable layer at the cloud base, a cloud layer and an inversion layer at the cloud

A regional real-time forecast of marine boundary layers during VOCALS-Rex

S. Wang et al.

[Title Page](#)[Abstract](#)[Introduction](#)[Conclusions](#)[References](#)[Tables](#)[Figures](#)[⏪](#)[⏩](#)[◀](#)[▶](#)[Back](#)[Close](#)[Full Screen / Esc](#)[Printer-friendly Version](#)[Interactive Discussion](#)

top (e.g., Albrecht et al., 1995; and Stevens, 2007). Because the shallow cumulus convection is driven by small-scale turbulent flows, it cannot be explicitly and realistically simulated by the 15 km grid mesh. Therefore, a shallow cumulus parameterization like that developed by Park and Bretherton (2009) or by Golaz et al. (2002) should be implemented in COAMPS to address the issue of the grid-scale shallow convection.

Direct comparison of four predicted variables with the RHB observations are plotted in Fig. 11. Below 500 m or above 2.2 km, biases in θ and q_v are about -0.8 K and 0.8 g kg^{-1} , respectively, and bias in u and v is less than 1 m s^{-1} . Because the predicted z_i is in general lower than the RHB, θ has a positive bias (3.5 K) and q_v has a negative bias (-0.7 g kg^{-1}). Note that errors in the location of the inversion alias into errors in θ and q_v .

In summary, the COAMPS model forecast captures the basic large-scale variability of the MBL along 20° S, including the general increase in the MBL heights toward the open ocean, the more decoupled MBL structure offshore and the directional wind shear near the coast. The upward slope of the MBL height toward the west is consistent with the decrease in meridional wind speed across the inversion based on the thermal wind relationship. The analysis of the instantaneous and averaged MBL structure suggest that the sporadic features in the cloud field (e.g. Fig. 4a and 9b) is likely a result of the lack of shallow cumulus convection parameterization in the model. The comparisons with RHB and aircraft soundings consistently show a relatively large underprediction of the MBL heights in the nearshore area, which may adversely impact the cloud prediction. We show in Sect. 7 that this underprediction in MBL heights near the coast by the model, in part, result from the coarse horizontal and vertical resolution, which notably affect the vertical motion and horizontal advection associated with steep slope of the Andes.

A regional real-time forecast of marine boundary layers during VOCALS-Rex

S. Wang et al.

[Title Page](#)[Abstract](#)[Introduction](#)[Conclusions](#)[References](#)[Tables](#)[Figures](#)[⏪](#)[⏩](#)[◀](#)[▶](#)[Back](#)[Close](#)[Full Screen / Esc](#)[Printer-friendly Version](#)[Interactive Discussion](#)

5 Surface statistics

This section focuses on the evaluation of predicted surface variables with the observations collected with the RHB cruises and at the WHOI buoy moored at 20° S, 85° W. Figure 12 displays longitudinal variations of surface variables from the RHB observations and model forecast data. To better display the general trend of the variables, we first average the data into 1-degree longitude bins and then average them over each group. The temperature, wind speed and water vapor mixing ratio are measured at 15–18 m height on the RHB, and therefore they are converted to the 10-m level temperature according to the Monin-Obuhkov Similarity theory. The model SST closely follows the RHB SST variation, reaching local minimum values near 78° W and 75° W and increasing toward the coast as well as the open ocean. This pattern results in a minimum surface buoyancy flux near 78° W. It is also, in part, responsible for the strong lower tropospheric stability there (Fig. 9d). Reflecting the SST variation, both the predicted and RHB 10-m air temperature (T_{10m}) have low values near 78° W and 75° W. The modeled SST and T_{10m} have biases of 0.22 and -0.67°C , respectively, and correlation coefficients of 0.83 and 0.71, respectively, showing good agreement with the observations. The predicted q_{v10m} shown in Fig. 12c follows the RHB near the coast and shows a general increasing trend toward the open ocean. However, the overall correlation is low (0.25) and the bias is 0.44 g kg^{-1} . Being consistent with the RHB data, the predicted wind speed increases from 4 m s^{-1} nearshore to 7 m s^{-1} at 84° W. Its local variation is also comparable with the RHB observations. The wind speed has a low bias (-0.31 m s^{-1}) and a relatively high correlation coefficient of 0.76.

The COAMPS forecasts are also evaluated against those observed at the WHOI buoy located at 85° W and 20° S. The comparison statistics are presented in Table 1. The temperature and wind statistics are in general very similar to previous analyses over the area along the US west coast (e.g., Doyle et al., 2009). The temperature appears to be the best performing variable as both its bias and RMS error are low, even though its correlation coefficient is lower than the one calculated using the RHB

A regional real-time forecast of marine boundary layers during VOCALS-Rex

S. Wang et al.

Title Page

Abstract

Introduction

Conclusions

References

Tables

Figures



Back

Close

Full Screen / Esc

Printer-friendly Version

Interactive Discussion

data (Fig. 11).

The shortwave (SW) downward radiative flux from the forecasts has large RMS error compared to the buoy observations, suggesting that the cloud-radiation interaction is not well simulated. The longwave (LW) downwelling flux at the surface correlates poorly with that observed at the buoy (0.2 in Table 1).

To better understand the model radiative flux error, we further examine scatter plots of the LW fluxes between the forecasts and the observations collected at both the RHB and WHOI buoy (Fig. 13). Each scatter plot displays a “square” pattern with very similar corresponding values at the four corners. Presence of clouds would significantly increase the downward LW flux. Particularly, when the cloud layer is thick enough to radiate as a blackbody, the thermal radiation by the cloud is saturated and depends only on the cloud layer temperature. To examine the effects of clouds, we separate the “thick clouds” data points from “clouds free” ones using LWP from COAMPS and those measured by the RHB thermal infrared radiometer. The “thick cloud” condition is defined here as LWP greater than 30 g m^{-2} for both the observations and the forecasts; the “clouds free” is defined as LW less than 1 g m^{-2} for both data sets. These definitions are chosen because they successfully stratify the data.

As shown in Fig. 13a, the blue cluster at the upper-right corner of the “square” corresponds to the condition where both the observations and COAMPS forecasts are designated as “thick clouds”, while the green cluster at the lower-left corner indicates the “clouds free” condition. We also take an average of all RHB measured clear-sky downward LW fluxes and obtain the value 315 W m^{-2} which is close to the values within the “clouds free” circle. It is noticeable that the majority of the “blue” and “green” data points are located along the one-to-one correlation line. Therefore, the LW radiative fluxes for both the “clouds free” and “thick clouds” conditions are well simulated by the model. These clusters of points account for 50% of all data points (117 out of 235 total). Errors occur when cloud conditions are very different between the forecast and observation datasets. For example, the points at the upper-left corner with values centered at (320, 380) represent the “clouds free” condition in the observations and the “thick

A regional real-time forecast of marine boundary layers during VOCALS-Rex

S. Wang et al.

Title Page

Abstract

Introduction

Conclusions

References

Tables

Figures



Back

Close

Full Screen / Esc

Printer-friendly Version

Interactive Discussion



clouds” in the COAMPS forecasts. The points along the right-hand-side vertical line of the square (i.e., $RHB \approx 380 \text{ W m}^{-2}$) indicate that the “thick clouds” conditions from the RHB are associated with thin cloud or partial cloudiness conditions in the model. This LW comparison raises two issues related to the cloud-radiation interaction modeling.

- 5 One is the realistic prediction of q_c and partial cloudiness; the other is the physical representation of these cloud variables in the radiation calculation. Both issues need to be further addressed to improve the radiation modeling in the future.

6 Diurnal variation of marine boundary layer structure

Section 2 presents the regional cloud variation of the MBL diurnal cycle as derived from both the model forecasts and satellite data. This section focuses on the comparison between the forecast and observed diurnal cycle of MBL structure. RHB rawindsondes were launched six times daily at approximately 00:00, 04:00, 08:00, 12:00, 16:00, and 20:00 UTC. These measurements provide adequate sampling of the diurnal variation of the MBL structure. The model forecast soundings are averaged at the observation times to produce the mean diurnal cycles for both the forecasts and the RHB observations. To reduce the effects of the longitudinal variations of MBL heights, we normalize the sounding profiles using the MBL heights before averaging.

As shown in Fig. 14, both the MBL heights (z_i) calculated from the RHB and the model undergo a well-defined diurnal cycle with the maximum in the morning and the minimum in the afternoon. This diurnal cycle is consistent with our general understanding that the daytime solar cloud absorption tends to suppress turbulent intensity and reduce cloud amount, leading to weaker cloud-top entrainment and a shallower boundary layer. Both the forecast and the observed z_i reach the maximum around 06:00 LST. The RHB z_i obtains its minimum at 15:00 LST, 4 h earlier than in the forecasts. The RHB z_i is, on average, 140 m higher than in the forecasts. Its diurnal amplitude is 130 m compared to only 60 m for that of the COAMPS z_i , which is consistent with our earlier result that the diurnal amplitude of the satellite LWP is in general larger than the

A regional real-time forecast of marine boundary layers during VOCALS-Rex

S. Wang et al.

Title Page

Abstract

Introduction

Conclusions

References

Tables

Figures



Back

Close

Full Screen / Esc

Printer-friendly Version

Interactive Discussion



COAMPS as shown in Fig. 4.

Figure 15 compares the MBL structure from the RHB and the forecasts. To better present the results, we only show the profiles at 06:54, 14:50 and 22:30 LST. The general trend of the MBL warming during the daytime is the same in both the forecasts and the RHB observations, as shown by the θ profiles in Fig. 15a and b. The MBL temperature increases with the cloud-layer solar warming during the daytime, creating a more stratified structure at 14:50 LST. In the evening, the cloud layer cools down as the cloud solar warming diminishes and the cloud-top longwave cooling dominates again. There are clear differences in the θ profiles between the observed and predicted at 14:50 LST. The RHB θ demonstrates a three-layered structure with a thin stable layer at $0.6 z/z_i$, separating the upper stratocumulus clouds from the surface-based subcloud layer. The COAMPS θ profile has a smoothly transitioned two-layered (cloud and subcloud layer) structure. These differences suggest that the daytime predicted MBL has a less decoupled structure, which is consistent with the fact that the cloud layer warming shown in the forecast soundings (0.6 K between 07:00 and 14:50 LST) is less than that from the RHB (0.8 K).

The COAMPS q_v is larger in general and has less diurnal variation than the RHB, as shown in Fig. 15c and d. A two-layer structure for all the COAMPS q_v soundings is clearly seen with the subcloud layer being nearly well-mixed. In contrast, the RHB q_v profile has a multi-layered structure at 14:45 LST, being consistent with the RHB θ profile at the same time. The maximum diurnal change in q_v from the COAMPS is only 0.25 g kg^{-1} compared to 0.5 g kg^{-1} from the RHB soundings.

Associated with these diurnal changes in the predicted θ and q_v , the q_c and TKE also undergo similar corresponding changes, as shown in Fig. 15e and f. The q_c maximum is 0.35 g kg^{-1} at 06:54 LST, and decreases to 0.15 g kg^{-1} at 14:45 LST. The lower cloud layer with small q_c represents shallow cumulus clouds underneath the main stratocumulus layer between 0.6 and $1 z/z_i$. A significant reduction in TKE from early morning to afternoon is apparent, particularly in the cloud layer (Fig. 15d). The minimum values of the TKE profiles near the mid-MBL indicate that the cloud layer

A regional real-time forecast of marine boundary layers during VOCALS-Rex

S. Wang et al.

Title Page

Abstract

Introduction

Conclusions

References

Tables

Figures

⏪

⏩

◀

▶

Back

Close

Full Screen / Esc

Printer-friendly Version

Interactive Discussion



Discussion Paper | Discussion Paper | Discussion Paper | Discussion Paper | Discussion Paper

tends to decouple from the subcloud layer.

7 Sensitivity of MBL structure to grid resolution

The evaluation of the COAMPS forecasts shows that the MBL heights close to the coast are significantly lower than in the observations (Figs. 7 and 9). This deficiency appears to be quite common among many global and regional models as discussed by Wyant et al. (2010). This consistent bias among the models promotes us to further analyze the prediction results at different horizontal as well as vertical resolutions.

We first compare the averaged MBL structure on three nested grid meshes (45 km, 15 km, and 5 km) at two locations: nearshore at 72° W and 20° S, and offshore at 76° W and 20° S. The MBL height at the nearshore location increases by 250 m and the temperature by 1 K at 72° W by increasing the horizontal resolution from 45 km to 5 km (Fig. 16). Correspondingly, q_c increases by 50% to 0.15 g kg^{-1} at the 3rd grid mesh (5 km). The higher-resolution grid clearly tends to improve the predicted MBL structure and clouds at the nearshore location. On the contrary, the higher-resolution nest has little impact on the MBL structure at the offshore location. This difference implies that the improvement for the nearshore MBL is likely caused by changes in mesoscale motions due to the high-resolution grid.

Figure 16 further shows that changes in downward motion and θ horizontal advection between the coarse and fine resolution grids are likely responsible for these structural changes at 72° W and 20° S. The finest-resolution mesh (5 km) results in the weakest subsidence at the MBL height, leading to the highest MBL height among the three grid meshes. The horizontal θ advection in the 45 km grid mesh gives the largest cooling rate near the surface; double that from the other grid meshes. Consequently, this large horizontal advective cooling and strong divergence tend to strengthen the cloud-top inversion and limit the MBL growth, resulting in the lowest MBL height in the 45 km grid mesh. It is also noticed that the subsidence and the total advection heating are very similar among the three grid meshes at 76° W and 20° S, which is consistent with the

A regional real-time forecast of marine boundary layers during VOCALS-Rex

S. Wang et al.

Title Page

Abstract

Introduction

Conclusions

References

Tables

Figures



Back

Close

Full Screen / Esc

Printer-friendly Version

Interactive Discussion



similar MBL heights predicted at the offshore location.

Effects of vertical resolution on the forecast MBL are also evaluated by conducting another model simulation with an enhanced vertical resolution of 95 levels (50 levels below 2 km) compared to the 45 (23 levels below 2 km) in the real-time forecast. Both vertical resolutions are tested with each of the three horizontal resolution grids discussed above. The 48-h sensitivity simulation is initialized at 00:12 Z on 22 October 2008 and its time-averaged results are shown in Fig. 17. Apparent in the figure is that the increase in the vertical resolution leads to increases of MBL heights for all three grids near the coast with the impact on the 5 km grid being the greatest. The increased vertical resolution has little impact on the MBL structure offshore (not shown here). Associated with the increase in the MBL height, turbulence intensity becomes stronger, particularly near the MBL top. This result is likely caused by enhanced radiative cooling induced by larger cloud water mixing ratio. Fig. 17 also makes an important point that the high-vertical resolution produces weaker subsidence in the MBL than the control forecast for all three grids. For the 5 km mesh, the high-resolution simulation gives the weakest subsidence and produces the highest MBL height. There is therefore a clear correlation between the increased MBL heights and the weakened subsidence within and just above the MBL produced by the increased vertical and horizontal resolution meshes.

The above results suggest that the increases in both the horizontal and vertical resolutions lead to the improvements in the simulated MBL heights and clouds near the coast, and these improvements may come from better defined coastal circulations. The increase in horizontal resolution helps better resolve the topography and coastal flows. The increase in the vertical resolution may have reduced numerical errors associated with some gradient calculation near a steep slope. This is consistent with some previous studies demonstrating that numerical treatment of mountain slopes is critical for a realistic simulation of local mesoscale circulations (e.g., Zängl, 2002). However, the details about the dependence of coastal mesoscale circulations on the model resolutions and numerical techniques are beyond the scope of this study.

A regional real-time forecast of marine boundary layers during VOCALS-Rex

S. Wang et al.

Title Page

Abstract

Introduction

Conclusions

References

Tables

Figures



Back

Close

Full Screen / Esc

Printer-friendly Version

Interactive Discussion



8 Summary

COAMPS was employed to provide twice-daily 48 h forecasts during VOCALS-Rex in October and November 2008. The model was configured to contain three nested grid meshes (45 km, 15 km and 5 km) with 45 vertical levels to cover the large experiment area with adequate resolution. The MBL structure from the real-time forecasts are evaluated and validated against observations taken on a number of platforms, including aircraft, ship, buoy and satellite operating in the region.

The regional distributions of the 41-day averaged forecasted LWP and wind speed are generally in agreement with those observed by satellite, although the modeled LWP is slightly smaller and wind speed larger in the VOCALS-Rex region. The overall location, direction and strength of the southerly coastal jet along the Chilean coast are correctly predicted. The harmonic regression analysis shows that the phase of diurnal variation of the MBL clouds and the surface wind speed are consistent with the satellite data. The diurnal amplitude of the predicted LWP exhibits a spotty spatial distribution compared to the smooth distribution of the satellite data. We have shown that this spotty distribution is caused by grid shallow convection due to a lack of a shallow cumulus convection parameterization in the model. The diurnal correlation coefficient derived from the forecasts is notably less than the values derived from the satellite data. There is strong indication that these deficiencies are linked to the lack of a shallow cumulus convection parameterization in COAMPS.

The forecast-observation comparisons along 20° S demonstrate overall consistency in some basic MBL characteristics, including a general upward slope in the MBL height, a more decoupled boundary layer structure toward the west, and maximum wind speeds near the top of the MBL. Both the forecasts and the observations show a trend of decreasing moisture above the MBL away from the coast; this trend is consistent with the upward slope of the MBL height as the drier air aloft tends to result in stronger radiative cooling near the cloud tops and therefore promotes more turbulence and a deeper MBL offshore. The model analyzed SST, forecasted 10-m air temperature

A regional real-time forecast of marine boundary layers during VOCALS-Rex

S. Wang et al.

Title Page

Abstract

Introduction

Conclusions

References

Tables

Figures



Back

Close

Full Screen / Esc

Printer-friendly Version

Interactive Discussion



A regional real-time forecast of marine boundary layers during VOCALS-Rex

S. Wang et al.

Title Page

Abstract

Introduction

Conclusions

References

Tables

Figures

⏪

⏩

◀

▶

Back

Close

Full Screen / Esc

Printer-friendly Version

Interactive Discussion



and surface wind speed yield realistic zonal variations along 20° S compared with ship-based RHB observations. The model consistently predicted a shallower MBL (~700 m) than what was observed (~1100 m) in the coastal region. This bias leads to an overall low cloud water mixing ratio in the model forecasts compared to the observations. The overall statistical errors of the surface wind speed and temperature are consistent with previous analyses (e.g., Doyle et al., 2009), with the wind speed bias ($<0.35 \text{ m s}^{-1}$) and RMS (1.3 m s^{-1}) and the temperature bias (-0.7 K) and RMS (0.5 K).

The forecasted LW on both the “thick cloud” and “clouds free” conditions produce good agreements with the observed values, but the forecasted LW suffers when the prediction of clouds is in error, suggested by the “square” patterns on the model-observation LW scatter plots. This clearly shows the importance of the accurate prediction of cloud water mass and fractional coverage in the determination of LW radiative fluxes.

COAMPS also predicted a well-defined diurnal variation in the temporally and spatially averaged MBL structure, which is generally consistent with the RHB observed z_i , θ and q_v . The forecasted mean structure, however, has smaller diurnal changes in these variables compared to the observations; this feature is also reflected in the smaller diurnal amplitude in the regional LWP diurnal harmonic analysis. The current study does not include the diurnal variability that is driven by the upsidence wave. This diurnal variability is discussed in detail by Rahn and Garreaud (2010) using model simulations and observations in VOCALS-Rex.

To further understand the underprediction of MBL heights near the coast, we examined the impacts of the model resolution. It was found that higher-resolutions in both the horizontal and vertical directions indeed have noticeable positive impacts on the nearshore MBL heights, while having little influence offshore. The 5-km grid mesh (45 vertical levels) predicted higher and more realistic MBL height (~900 m) than the 15 km mesh (~700 m) or the 45 km mesh (~600 m). Enhancing the vertical resolution to 95 levels further increased the MBL height to 1100 m for the 5 km grid. These improvements are likely due to the changes to the mesoscale flows such as the reduced

coastal downward motion and weakened cold advection near the surface produced by the high-resolution forecasts. Given the generality of this bias among regional and global models, and the implications of the resolution study in this work, efforts should be directed to improve simulations of mesoscale flows under the influence of steep terrains.

Acknowledgements. This work was supported by the Office of Naval Research (ONR) under Program Element (PE) 0602435N and by National Science Foundation (ATM-0749011). The first author thanks NRL COAMPS-On Scene group for their support for the COAMPS forecast during VOCALS-Rex. COAMPS[®] is a registered trademark of the Naval Research Laboratory.

References

- Albrecht, B. A.: Aerosols, cloud microphysics, and fractional cloudiness, *Science*, 245, 1227–1230, 1989.
- Albrecht, B. A., Jensen, M. P., and Syrett, W. J.: Marine boundary layer structure and fractional cloudiness, *J. Geophys. Res.*, 100, 14209–14222, 1995.
- Bony, S. and Dufresne, J.-L.: Marine boundary layer clouds at the heart of tropical cloud feedback uncertainties in climate models, *Geophys. Res. Lett.*, 32, L20806, doi:10.1029/2005GL023851, 2005.
- Bretherton, C. S., McCaa, J. R., and Grenier, H.: A new parameterization for shallow cumulus convection and its application to marine subtropical cloud-topped boundary layers. Part I: Description and 1D results, *Mon. Weather Rev.*, 132, 864–882, 2004.
- Bretherton, C. and Wyant, M. C.: Moisture transport, lower-tropospheric stability, and decoupling of cloud-topped boundary layers, *J. Atmos. Sci.*, 54, 148–167, 1997.
- Burk, S. D. and Thompson, W. T.: A vertically nested regional numerical weather prediction model with second-order closure physics, *Mon. Weather Rev.*, 117, 2305–2324, 1989.
- Cummings, J.: Operational multivariate ocean data assimilation, *Q. J. Roy. Meteor. Soc.*, 131, 3583–3604, 2005.
- de Zoete, S. P., Fairall, C. W., Zuidema, P., Wolfe, D. E., and Bariteau, L.: Surface flux observations on the southeastern tropical Pacific Ocean and attribution of SST errors in coupled ocean-atmosphere models, *J. Climate*, 23, 4152–4174, 2010.

A regional real-time forecast of marine boundary layers during VOCALS-Rex

S. Wang et al.

Title Page

Abstract

Introduction

Conclusions

References

Tables

Figures



Back

Close

Full Screen / Esc

Printer-friendly Version

Interactive Discussion



A regional real-time forecast of marine boundary layers during VOCALS-Rex

S. Wang et al.

Title Page

Abstract

Introduction

Conclusions

References

Tables

Figures

◀

▶

◀

▶

Back

Close

Full Screen / Esc

Printer-friendly Version

Interactive Discussion



de Szoeke, S. P., Wang, Y., Xie, S.-P., and Miyama, T.: Effect of shallow cumulus convection on the eastern Pacific climate in a coupled model, *Geophys. Res. Lett.*, 33, L17713, doi:10.1029/2006GL026715, 2006.

Doyle, J. D., Jiang, Q., Chao, Y., and Farrara, J.: High-resolution real-time modeling of the marine atmospheric boundary layer in support of the AOSN-II field campaign, *Deep-Sea Res. Pt. II*, 52, 87–99, doi:10.1016/j.dsr2.2008.08.009, 2009.

Felsch, P. and Whitlatch, W.: Stratus surge prediction along the central California coast, *Mon. Weather Rev.*, 8, 204–213, 1993.

Fu, Q. and Liou, K. N.: On the Correlated k -Distribution Method for Radiative Transfer in Non-homogeneous Atmospheres, *J. Atmos. Sci.*, 49, 2139–2156, 1992.

Garreaud, R. D. and Muñoz, R. C.: The diurnal cycle in circulation and cloudiness over the subtropical southeast pacific: a modeling study, *Mon. Weather Rev.*, 17, 1699–1710, 2004.

Garreaud, R. D. and Muñoz, R. C.: The low-level jet off the west coast of subtropical South America: Structure and variability, *Mon. Weather Rev.*, 133, 2246–2261, 2005.

Golaz, J.-C., Larson, V. E., and Cotton, W. R.: A PDF-based model for boundary layer clouds. Part I: Method and model description, *J. Atmos. Sci.*, 59, 3540–3551, 2002.

Hignett, P.: Observations of diurnal variation in a cloud-capped marine boundary layer, *J. Atmos. Sci.*, 48, 1474–1482, 1991.

Hodur, R. M.: The Naval Research Laboratory's coupled ocean/atmosphere mesoscale prediction system (COAMPS), *Mon. Weather Rev.*, 125, 1414–1430, 1997.

Jiang, Q., Wang, S., and O'Neill, L.: Some insights into the characteristics and dynamics of Chilean low-level coastal jet, *Mon. Weather Rev.*, in press, 2010.

Kain, J. S., and Fritsch, M.: A one-dimensional entraining/detraining plume model and its application in convective parameterization, *J. Atmos. Sci.*, 47, 2784–2802, 1990.

Klein, S. A.: Synoptic variability of low-cloud properties and meteorological parameters in the subtropical trade wind boundary layer, *J. Climate*, 10, 2018–2039, 1997.

Klein, S. A. and Hartmann, D. L.: The seasonal cycle of low stratiform clouds, *J. Climate*, 6, 1587–1606, 1993.

Klein, S. A., Hartmann, D. L., and Norris, J. R.: On the relationships among low-cloud structure, sea surface temperature, and atmospheric circulation in the summertime northeast Pacific, *J. Climate*, 8, 1140–1155, 1995.

Lilly, D. K.: Models of cloud-topped mixed layers under a strong inversion, *Q. J. Roy. Meteor. Soc.*, 94, 292–308, 1968.

A regional real-time forecast of marine boundary layers during VOCALS-Rex

S. Wang et al.

Title Page

Abstract

Introduction

Conclusions

References

Tables

Figures

⏪

⏩

◀

▶

Back

Close

Full Screen / Esc

Printer-friendly Version

Interactive Discussion



- Liu, M., Nachamkin, J. E., and Westphal, D. L.: On the improvement of COAMPS weather forecasts using an advanced radiative transfer model, *Weather Forecast.*, 24, 286–306, 2009.
- Louis, J. F., Tiedtke, M., and Geleyn J. F.: A short history of the operational PBL-parameterization of ECMWF, *Proceedings of the 1981 ECMWF workshop on planetary boundary layer parameterization*, Shinfield Park, Reading, Berkshire, UK, European Centre for Medium Range Weather Forecasts, 59–79, 1982.
- Lorenz, E. N.: Available energy and the maintenance of a moist circulation, *Tellus*, 30, 241–259, 1978.
- Ma, C.-C., Mechoso, C. R., Robertson A. W., and Arakawa, A.: Peruvian stratus clouds and the tropical Pacific circulation: a coupled ocean-atmosphere GCM study, *J. Climate*, 9, 1635–1645, 1996.
- McCaa, J. R. and Bretherton, C. S.: A new parameterization for shallow cumulus convection and its application to marine subtropical cloud-topped boundary layers. Part II: Regional simulations of marine boundary layer clouds, *Mon. Weather Rev.*, 132, 883–896, 2004.
- Mechem, D. B. and Kogan, Y. L.: Simulating the transition from drizzling marine stratocumulus to boundary layer cumulus with a mesoscale model, *Mon. Weather Rev.*, 131, 2342–2360, 2003.
- Mellor, G. L.: The Gaussian cloud model relations, *J. Atmos. Sci.*, 34, 356–358, 1977.
- Mellor, G. L. and Yamada, T.: Development of a turbulence closure for geophysical fluid problems, *Rev. Geophys. Space Ge.*, 20, 851–875, 1982.
- Mocko, D. M. and Cotton, W. R.: Evaluation of fractional cloudiness parameterizations for use in a mesoscale model, *J. Atmos. Sci.*, 52, 2884–2901, 1995.
- Muñoz, R. C. and Garreaud, R. D.: Dynamics of the low-level jet off the west coast of subtropical South America, *Mon. Weather Rev.*, 133, 3661–3667, 2005.
- Nicholls, S.: The dynamics of stratocumulus: aircraft observations and comparison with a mixed-layer model, *Q. J. Roy. Meteor. Soc.*, 112, 431–460, 1984.
- O'Dell, C. W., Wentz, F. J., and Bennartz, R.: Cloud liquid water path from satellite-based passive microwave observations: a new climatology over the global oceans, *J. Climate*, 8, 1721–1739, 2008.
- Palmen, E. and Newton, C. W.: *Atmospheric Circulation System*, Academic Press, 603 pp., 1969.
- Park, S. and Bretherton, C.: The University of Washington shallow convection and moist turbulence schemes and their impact on climate simulations with the community atmosphere

A regional real-time forecast of marine boundary layers during VOCALS-Rex

S. Wang et al.

Title Page

Abstract

Introduction

Conclusions

References

Tables

Figures

⏪

⏩

◀

▶

Back

Close

Full Screen / Esc

Printer-friendly Version

Interactive Discussion



model, *J. Climate*, 22, 3449–3469, 2009.

Rotunno, R.: On the linear theory of the land- and sea-breeze, *J. Atmos. Sci.*, 41, 1999–2009, 1983.

Rozendaal M. A., Leovy, C. B., and Klein, S. A.: An observational study of diurnal 41 variation of marine stratiform clouds, *J. Climate*, 8, 1795–1809, 1995.

Rutledge, S. A. and Hobbs, P. V.: The mesoscale and microscale structure of organization of clouds and precipitation in midlatitude cyclones. VIII: a model for the “seeder-feeder” process in warm-frontal rainbands, *J. Atmos. Sci.*, 40, 1185–1206, 1983.

Rutllant, J.: Coastal lows and associated southerly winds in North-Central Chile, Preprints, Fourth Int. Conf. on Southern Hemisphere Meteorology, Hobart, Australia, Amer. Meteor. Soc., 268–269, 1993.

Shulman, I., Kindle, J., Martin, P., deRada, S., Doyle, J., Penta, B., Anderson, S., Chavez, F., Paduan, J., and Ramp, S.: Modeling of upwelling/relaxation events with the Navy Coastal Ocean Model, *Deep-Sea Res. Pt. II*, 112, C06023, doi:10.1029/2006JC003946, 2007.

Siebesma, A. P., Soares, M. M., and Teixeira, J.: A combined eddy-diffusivity mass-flux approach for the convective boundary layer, *J. Atmos. Sci.*, 64, 1230–1248, 2007.

Sommeria, G. and Deardorff, J. W.: Subgrid-scale condensation in models of nonprecipitating clouds, *J. Atmos. Sci.*, 34, 344–355, 1977.

Stevens, B., Vali, G., Comstock, K., vanZanten, M. C., Austin, P. H., Bretherton, C. S., and Lenschow, D. L.: Pockets of open cells and drizzle in marine stratocumulus, *B. Am. Meteorol. Soc.*, 86, 51–57, 2005.

Stevens, B.: On the growth of layers of nonprecipitating cumulus convection, *J. Atmos. Sci.*, 64, 2916–2931, 2007.

Turton, J. D. and Nicholls, S.: A study of the diurnal variation of stratocumulus using a multiple mixed layer model, *Q. J. Roy. Meteor. Soc.*, 113, 969–1009, 1987.

Thompson, W. T., Burk, S. D., and Lewis, J.: Fog and low clouds in a coastally trapped disturbance, *J. Geophys. Res.*, 110, D18213, doi:10.1029/2004JD005522, 2005.

Wang, H. and Feingold, G.: Modeling mesoscale cellular structures and drizzle in marine stratocumulus. Part I: Impact of drizzle on the formation and evolution of open cells, *J. Atmos. Sci.*, 66, 3237–3256, 2009.

Wang, S., Albrecht, B. A., and Minnis P.: A regional simulation of marine boundary-layer clouds, *J. Atmos. Sci.*, 50, 4022–4043, 1993.

Wang, S., Wang, Q., and Doyle, J.: Some improvement of Louis surface flux parameteriza-

A regional real-time forecast of marine boundary layers during VOCALS-Rex

S. Wang et al.

Title Page

Abstract

Introduction

Conclusions

References

Tables

Figures



Back

Close

Full Screen / Esc

Printer-friendly Version

Interactive Discussion



tion, Preprints, 15th Symp. on Boundary Layers and Turbulence, Wageningen, Netherlands, Amer. Meteor. Soc., 547–550, 2002.

Wang, S., Golaz, J.-C., and Wang, Q.: Effect of intense wind shear across the inversion on stratocumulus clouds, *Geophys. Res. Lett.*, 35, L15814, doi:10.1029/2008GL033865, 2008.

5 Wang, Y., Xie, S.-P., Xu, H., and Wang, B.: Regional model simulations of marine boundary layer clouds over the southeast Pacific off South America. Part I: Control experiment, *Mon Weather Rev.*, 132, 274–296, 2004

10 Wang, Y., Xu, H., and Xie, S.-P.: Regional model simulations of marine boundary layer clouds over the southeast Pacific off South America. Part II: Sensitivity experiments, *Mon. Weather Rev.*, 132, 2650–2668, 2004

Wood, R., Bretherton, C., Huebert, B., Mechoso, C. R., and Weller, R.: VOCALS: The VAMOS Ocean-Cloud-Atmosphere-Land Study. http://www.eol.ucar.edu/projects/vocals/documentation/vocals_overview.pdf, 2007.

15 Wood, R., Köhler, M., Bennartz, R., and O'Dell, C.: The diurnal cycle of surface divergence over the global oceans, *Q. J. Roy. Meteor. Soc.*, 135, 1484–1493, 2009.

Wyant, M. C., Wood, R., Bretherton, C. S., Mechoso, C. R., Bacmeister, J., Balmaseda, M. A., Barrett, B., Codron, F., Earnshaw, P., Fast, J., Hannay, C., Kaiser, J. W., Kitagawa, H., Klein, S. A., Köhler, M., Manganello, J., Pan, H.-L., Sun, F., Wang, S., and Wang, Y.: The Pre-VOCA experiment: modeling the lower troposphere in the Southeast Pacific, *Atmos. Chem. Phys.*, 10, 4757–4774, doi:10.5194/acp-10-4757-2010, 2010.

20 Zängl, G.: An improved method for computing horizontal diffusion in a sigma-coordinate model and its application to simulations over mountainous topography, *Mon. Weather Rev.*, 130, 1423–1432, 2002.

A regional real-time forecast of marine boundary layers during VOCALS-Rex

S. Wang et al.

Table 1. Statistical parameters comparing the COAMPS forecasts with the WHOI buoy observations. Correlation coefficients in the last row do not have any units.

	T (K)	u (m s^{-1})	v (m s^{-1})	Speed (m s^{-1})	LW (W m^{-2})	SW (W m^{-2})
Bias	-0.43	-0.51	1.0	0.35	2.68	-7.74
RMS	0.47	1.54	1.66	1.35	26.02	188.68
Corr.	0.62	0.52	0.47	0.62	0.20	0.84

Title Page

Abstract

Introduction

Conclusions

References

Tables

Figures

⏪

⏩

◀

▶

Back

Close

Full Screen / Esc

Printer-friendly Version

Interactive Discussion

A regional real-time forecast of marine boundary layers during VOCALS-Rex

S. Wang et al.

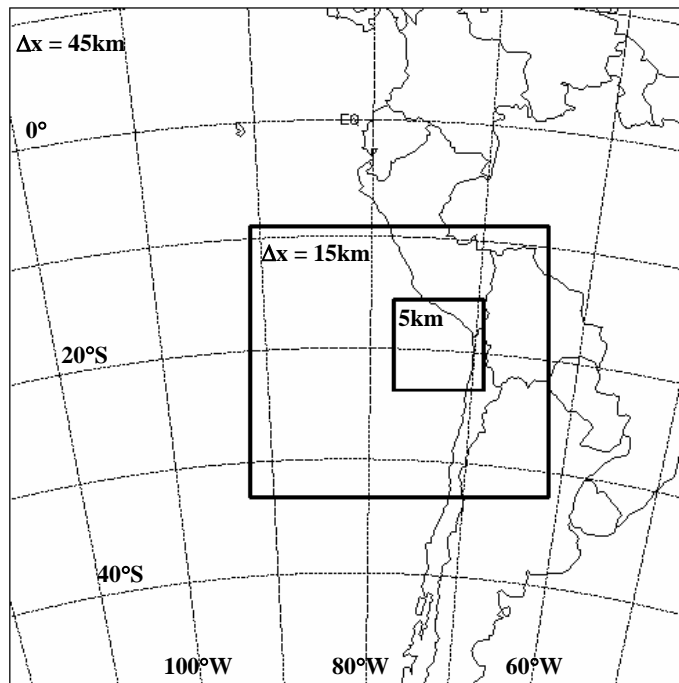


Fig. 1. COAMPS forecast domains for the VOCALS-Rex. Three grid meshes (45 km, 15 km, 5 km) have 151×151 , 199×188 , and 151×151 grid points, respectively.

[Title Page](#)[Abstract](#)[Introduction](#)[Conclusions](#)[References](#)[Tables](#)[Figures](#)[⏪](#)[⏩](#)[◀](#)[▶](#)[Back](#)[Close](#)[Full Screen / Esc](#)[Printer-friendly Version](#)[Interactive Discussion](#)

A regional real-time forecast of marine boundary layers during VOCALS-Rex

S. Wang et al.

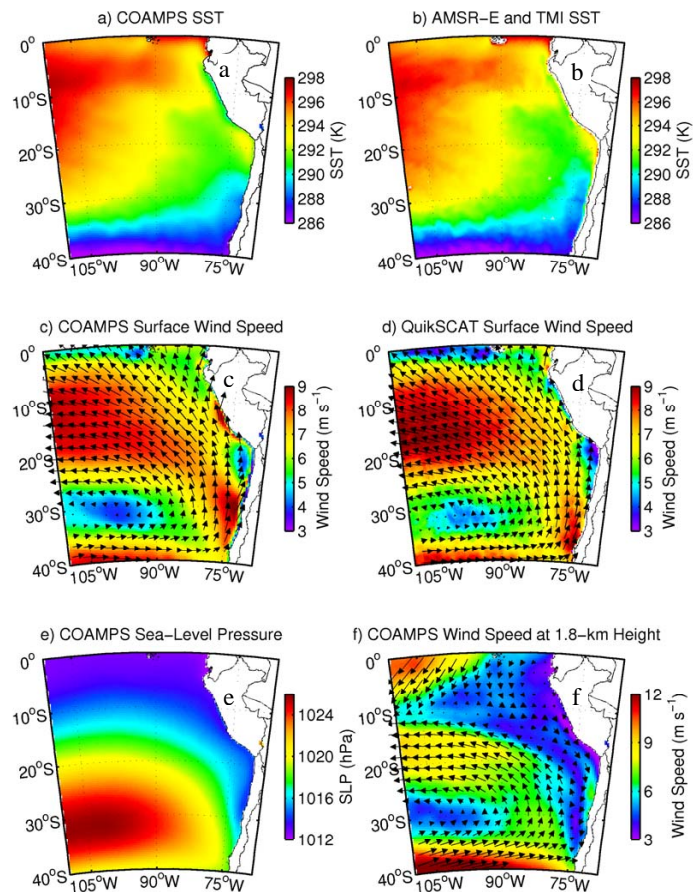


Fig. 2. Mean large-scale fields derived from the COAMPS forecasts (45 km grid) and the satellite data. **(a)** COAMPS SST; **(b)** AMSR-E and TMI SST; **(c)** COAMPS 10-m wind speed (color shading) and vectors; **(d)** QuickScat wind speed (color shading) and vectors; **(e)** COAMPS sea-level pressure; and **(f)** COAMPS 1.8 km wind speed (color shading) and vectors.

[Title Page](#)
[Abstract](#)
[Introduction](#)
[Conclusions](#)
[References](#)
[Tables](#)
[Figures](#)
[Back](#)
[Close](#)
[Full Screen / Esc](#)
[Printer-friendly Version](#)
[Interactive Discussion](#)

A regional real-time forecast of marine boundary layers during VOCALS-Rex

S. Wang et al.

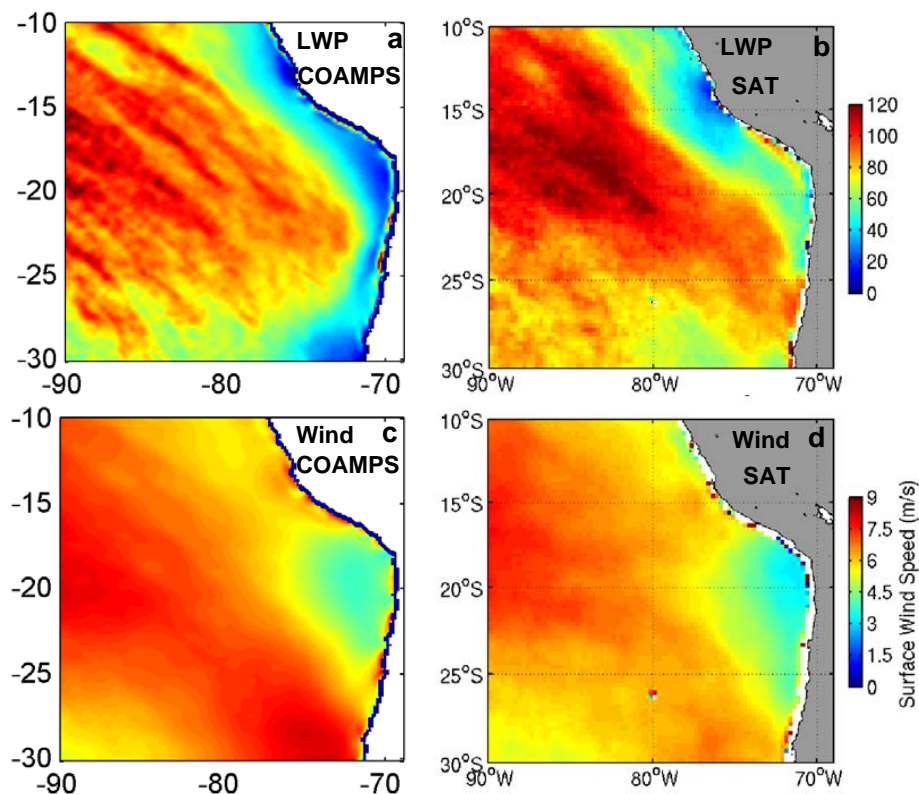


Fig. 3. Comparison of the mean LWP and wind speed between the COAMPS forecasts (15 km grid) and the satellite data. **(a)** COAMPS LWP; **(b)** satellite LWP; **(c)** COAMPS wind speed; and **(d)** satellite wind speed.

Title Page

Abstract

Introduction

Conclusions

References

Tables

Figures

◀

▶

◀

▶

Back

Close

Full Screen / Esc

Printer-friendly Version

Interactive Discussion

A regional real-time forecast of marine boundary layers during VOCALS-Rex

S. Wang et al.

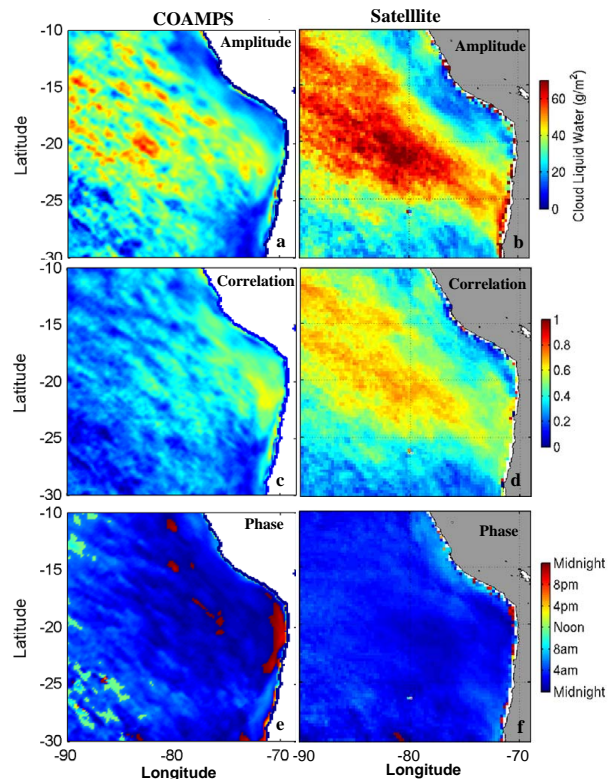


Fig. 4. Comparison of the harmonic analysis of LWP between the COAMPS forecasts (left column) and the satellite data (right column). **(a)** Forecasted diurnal amplitude; **(b)** satellite diurnal amplitude; **(c)** correlation with the predicted harmonic diurnal function; **(d)** correlation with the satellite diurnal function; **(e)** local hours of the LWP maximum in the model; and **(f)** local hours of the LWP maximum in the satellite data.

**A regional real-time
forecast of marine
boundary layers
during VOCALS-Rex**

S. Wang et al.

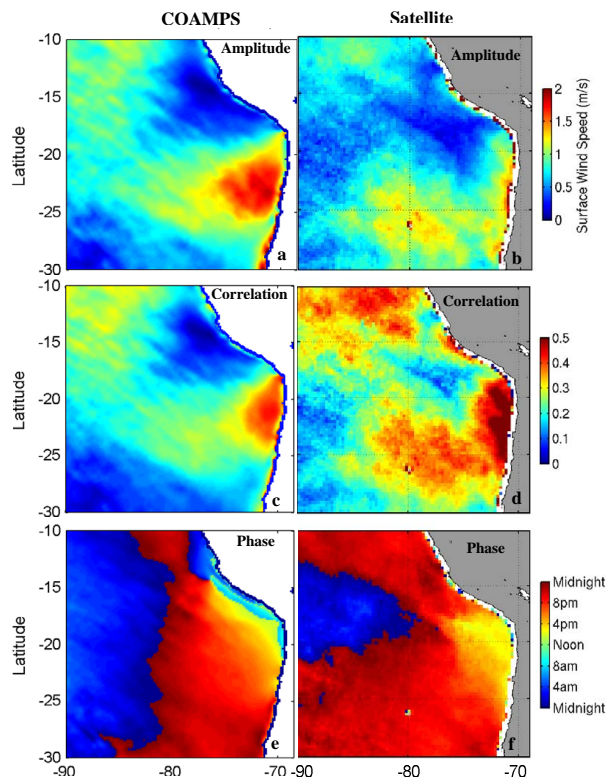


Fig. 5. The same as in Fig. 4 except for the surface wind speed.

Title Page

Abstract

Introduction

Conclusions

References

Tables

Figures

◀

▶

◀

▶

Back

Close

Full Screen / Esc

Printer-friendly Version

Interactive Discussion

A regional real-time forecast of marine boundary layers during VOCALS-Rex

S. Wang et al.

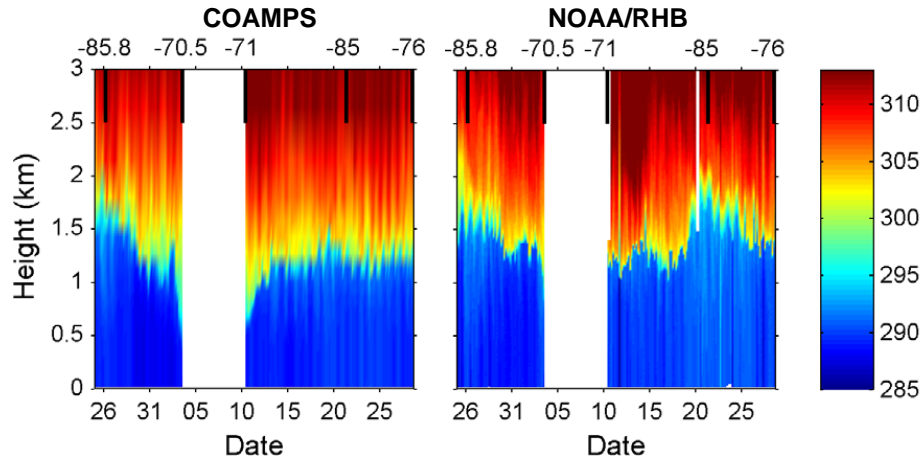


Fig. 6. Time-height cross-section of potential temperature (θ) from the COAMPS forecasts (left) and the RHB rawindsondes (right). The analysis covers the period of 25 October through 29 November 2008. The numbers at the upper axis with the heavy vertical lines denote the longitudes of the most western and eastern locations of the RHB cruise for each leg during this period. No data were collected 3–10 November between the two cruise legs.

Title Page

Abstract

Introduction

Conclusions

References

Tables

Figures

◀

▶

◀

▶

Back

Close

Full Screen / Esc

Printer-friendly Version

Interactive Discussion



A regional real-time forecast of marine boundary layers during VOCALS-Rex

S. Wang et al.

Composite COAMPS and RHB Soundings

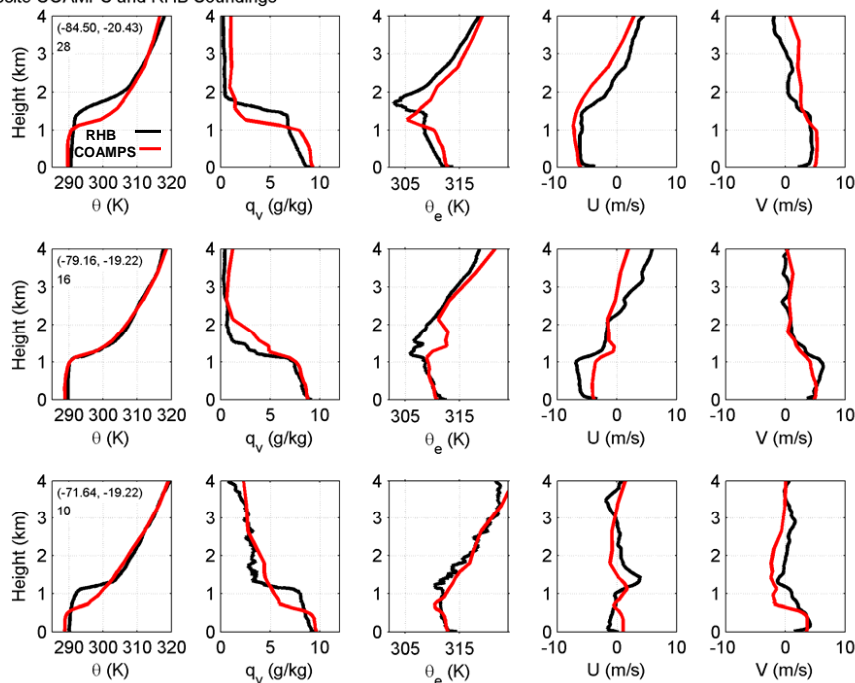


Fig. 7. Comparison of the composite COAMPS and RHB soundings. The soundings are averaged at the central location indicated by the pair of longitude and latitude in the first columns in the figure. The digits under the locations are the total number of soundings used in each averaging. The variables are denoted by x -axis labels. Red curves denote the forecast results; and the black the RHB.

[Title Page](#)
[Abstract](#)
[Introduction](#)
[Conclusions](#)
[References](#)
[Tables](#)
[Figures](#)
[⏪](#)
[⏩](#)
[◀](#)
[▶](#)
[Back](#)
[Close](#)
[Full Screen / Esc](#)
[Printer-friendly Version](#)
[Interactive Discussion](#)

A regional real-time forecast of marine boundary layers during VOCALS-Rex

S. Wang et al.

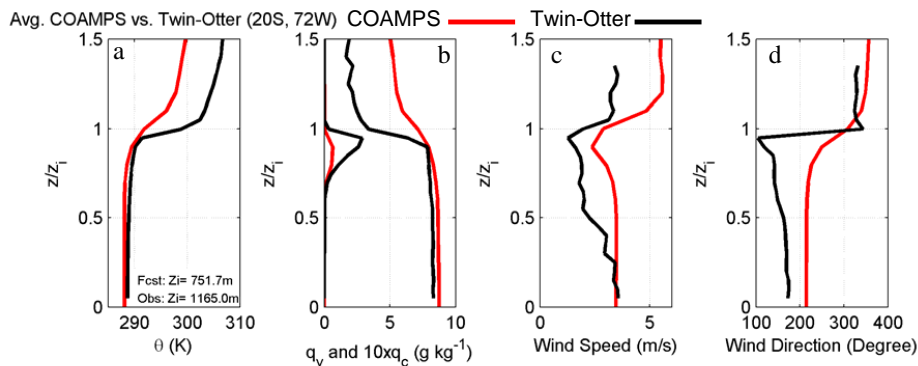


Fig. 8. Comparison between COAMPS and Twin Otter averaged soundings scaled by the boundary layer heights. **(a)** θ ; **(b)** q_v and $10 \times q_c$; **(c)** wind speed; and **(d)** wind direction.

[Title Page](#)
[Abstract](#)
[Introduction](#)
[Conclusions](#)
[References](#)
[Tables](#)
[Figures](#)
[◀](#)
[▶](#)
[◀](#)
[▶](#)
[Back](#)
[Close](#)
[Full Screen / Esc](#)
[Printer-friendly Version](#)
[Interactive Discussion](#)

A regional real-time forecast of marine boundary layers during VOCALS-Rex

S. Wang et al.

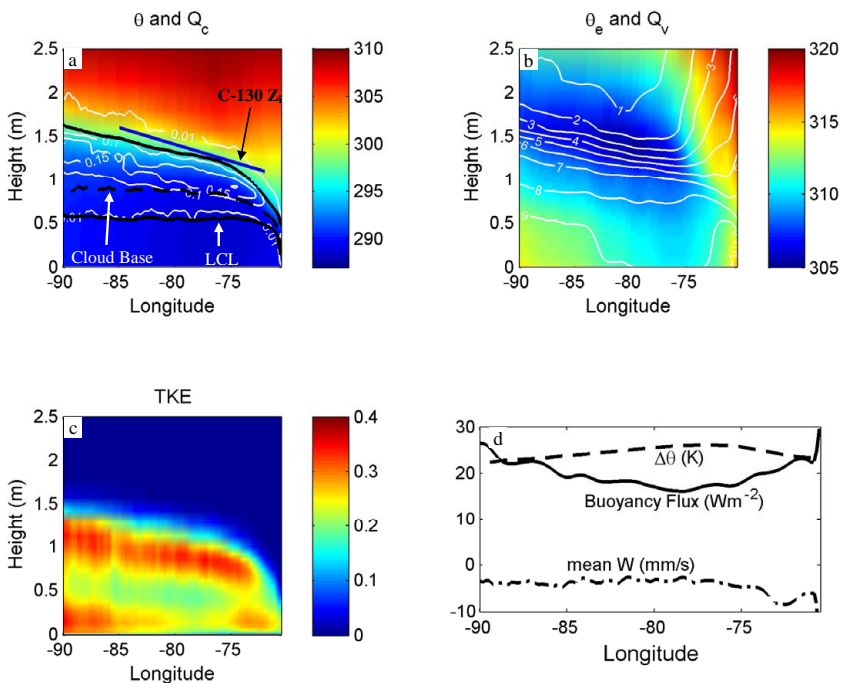


Fig. 9. COAMPS MBL variations along 20° S. **(a)** Longitude-height cross-section of q_c (white contours in g kg^{-1}) and θ (color shaded in K). The mean predicted MBL height is denoted by the upper branch of thick black curve, the mean LCL by the lower branch of the thick black curve, mean cloud base by the thick black dashed curve. The thick blue line is the MBL height fitted by C-130 data. **(b)** Cross-sections of q_v (white contours in g kg^{-1}) and θ_e (color shaded in K); **(c)** cross-section of the predicted TKE (in $\text{m}^2 \text{s}^{-2}$); and **(d)** predicted longitudinal variations of lower troposphere stability ($\Delta\theta = \theta_{3\text{km}} - \theta_{\text{SST}}$, dashed line in K), surface buoyancy flux (solid line in W m^{-2}) and time averaged vertical motion at the inversion height (dashed-dotted line in mm s^{-1}).

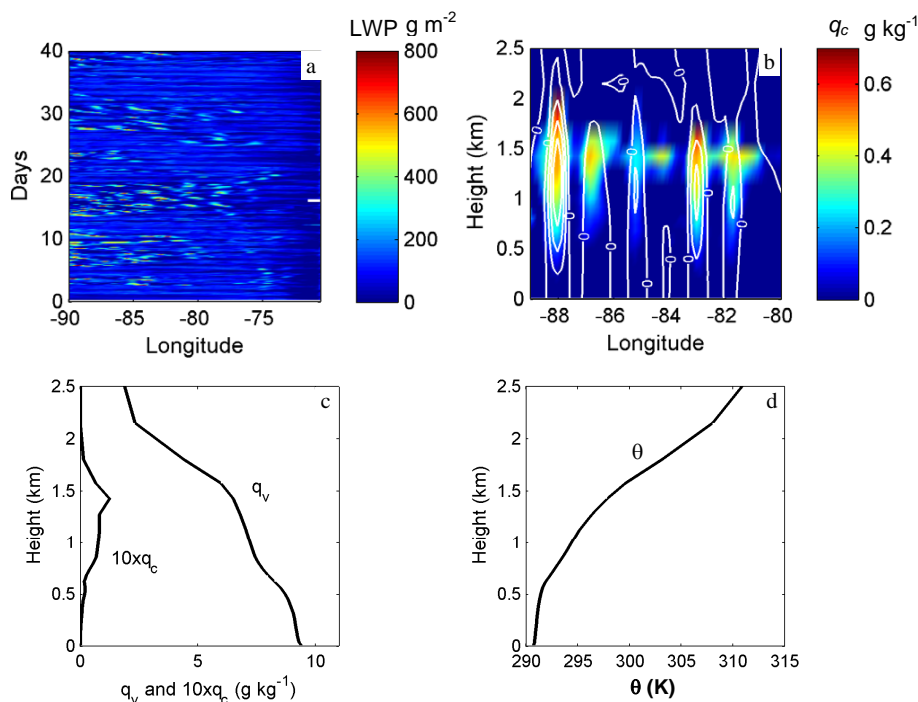


Fig. 10. Examples of grid-scale convection in the COAMPS simulation. **(a)** Longitude-time cross-section of the COAMPS LWP along 20° S, where time is denoted by the small white horizontal bar on the left vertical axis, **(b)** longitude-height cross-section of the instantaneous q_c (color shaded) and w (contours) along 20° S at 03:00 Z 5 November 2008. Contours for w start at 0 cm s^{-1} with an increment of 5 cm s^{-1} . **(c)** Mean profiles of q_v and q_c averaged between 89° W and 80° W; and **(d)** mean profile of θ .

Title Page

Abstract

Introduction

Conclusions

References

Tables

Figures

◀

▶

◀

▶

Back

Close

Full Screen / Esc

Printer-friendly Version

Interactive Discussion

A regional real-time forecast of marine boundary layers during VOCALS-Rex

S. Wang et al.

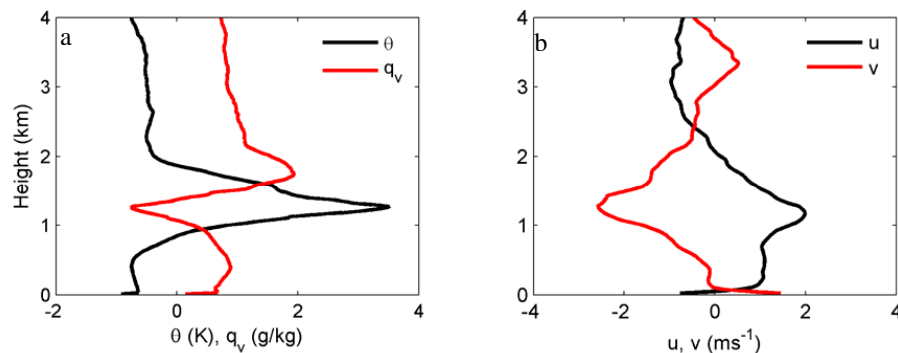


Fig. 11. COAMPS biases of the MBL profiles relative to the RHB observations. **(a)** θ and q_v ; and **(b)** u and v .

[Title Page](#)[Abstract](#)[Introduction](#)[Conclusions](#)[References](#)[Tables](#)[Figures](#)[◀](#)[▶](#)[◀](#)[▶](#)[Back](#)[Close](#)[Full Screen / Esc](#)[Printer-friendly Version](#)[Interactive Discussion](#)

A regional real-time forecast of marine boundary layers during VOCALS-Rex

S. Wang et al.

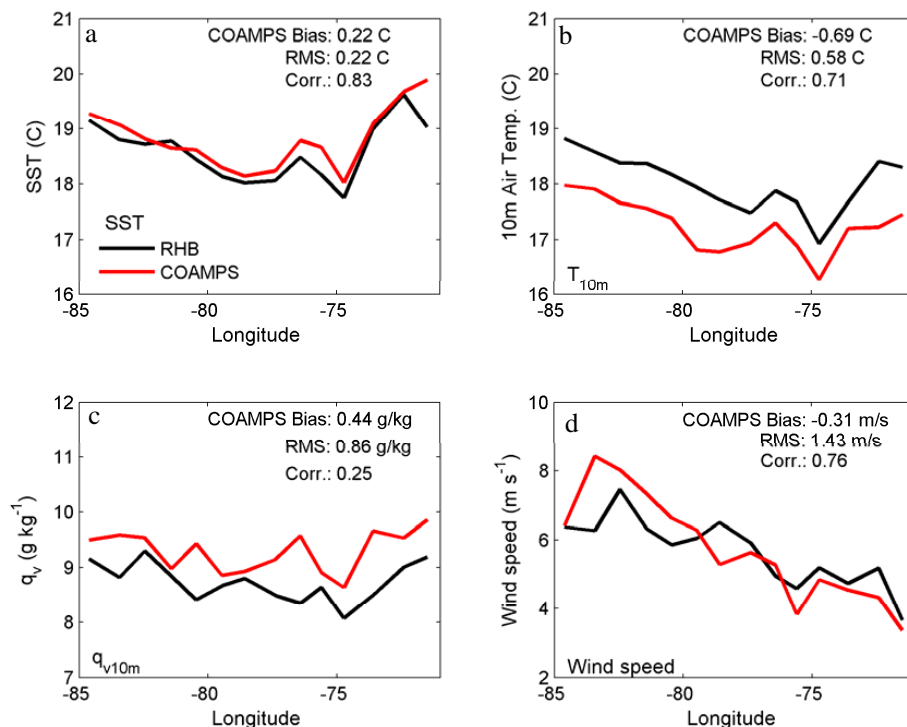


Fig. 12. Comparisons of longitudinal variations of **(a)** SST, **(b)** T_{10m} , **(c)** q_{v10m} , and **(d)** 10-m wind speed between the COAMPS forecasts and the RHB observations. All the plots are produced by averaging each variable into 1-degree longitude bins using the corresponding RHB and COAMPS data. The overall statistics (bias, RMS difference, and correlation coefficient) for the COAMPS-RHB comparisons are also displayed in each panel.

[Title Page](#)
[Abstract](#)
[Introduction](#)
[Conclusions](#)
[References](#)
[Tables](#)
[Figures](#)
[◀](#)
[▶](#)
[◀](#)
[▶](#)
[Back](#)
[Close](#)
[Full Screen / Esc](#)
[Printer-friendly Version](#)
[Interactive Discussion](#)

A regional real-time forecast of marine boundary layers during VOCALS-Rex

S. Wang et al.

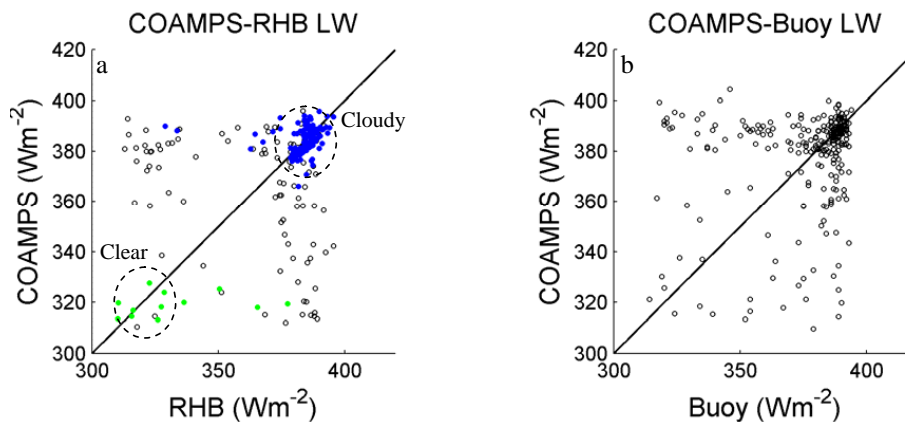


Fig. 13. Scatter plots of surface downward LW between observations and COAMPS forecasts. **(a)** COAMPS vs. RHB; and **(b)** COAMPS vs. Buoy. Solid green dots are the points with LWP less than 1 g m^{-2} from both the COAMPS and the RHB; solid blue dots are the points with LWP greater than 30 g m^{-2} from both the COAMPS and the RHB.

[Title Page](#)[Abstract](#)[Introduction](#)[Conclusions](#)[References](#)[Tables](#)[Figures](#)[◀](#)[▶](#)[◀](#)[▶](#)[Back](#)[Close](#)[Full Screen / Esc](#)[Printer-friendly Version](#)[Interactive Discussion](#)

A regional real-time forecast of marine boundary layers during VOCALS-Rex

S. Wang et al.

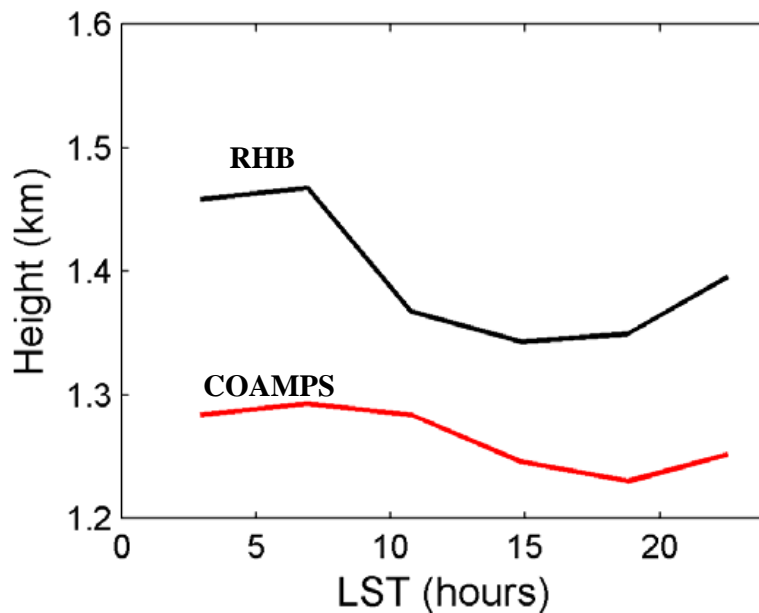


Fig. 14. Diurnal variations of mean MBL heights computed from the RHB soundings (black) and the COAMPS forecasts (red).

[Title Page](#)[Abstract](#)[Introduction](#)[Conclusions](#)[References](#)[Tables](#)[Figures](#)[◀](#)[▶](#)[◀](#)[▶](#)[Back](#)[Close](#)[Full Screen / Esc](#)[Printer-friendly Version](#)[Interactive Discussion](#)

A regional real-time forecast of marine boundary layers during VOCALS-Rex

S. Wang et al.

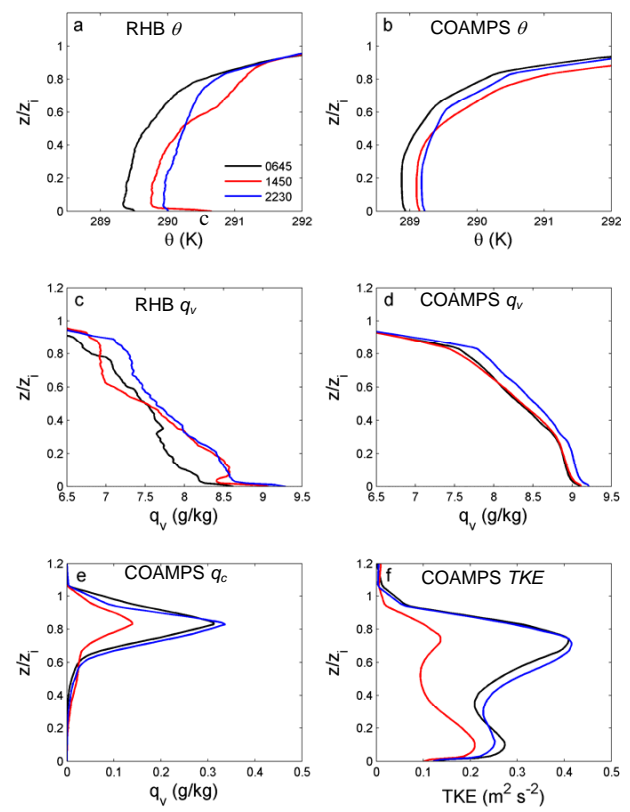


Fig. 15. Diurnal variation of normalized structures from the RHB observations and the COAMPS forecasts. **(a)** RHB θ ; **(b)** COAMPS θ ; **(c)** RHB q_v ; **(d)** COAMPS q_v ; **(e)** COAMPS q_c ; and **(f)** COAMPS TKE. The numbers in **(a)** denote local time of the soundings defined by the different colors.

Title Page

Abstract

Introduction

Conclusions

References

Tables

Figures

◀

▶

◀

▶

Back

Close

Full Screen / Esc

Printer-friendly Version

Interactive Discussion



A regional real-time forecast of marine boundary layers during VOCALS-Rex

S. Wang et al.

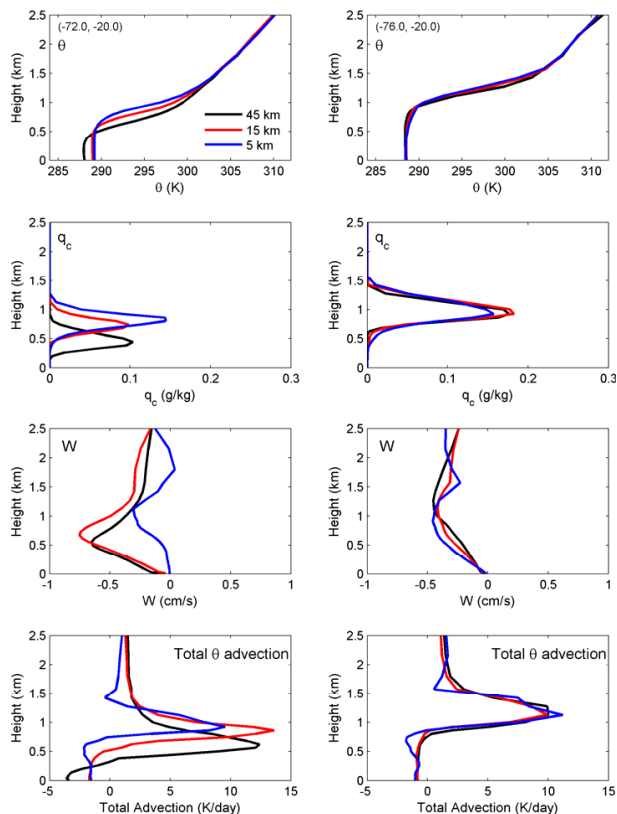


Fig. 16. Comparison of the averaged MBL structure and mesoscale forcing among the different resolution grids and locations. Left column of panels are results from the nearshore location at 72° W and 20° S; the right column the offshore location at 76° W and 20° S; The horizontal resolution (45 km, 15 km, 5 km) is denoted in the top-right panel. The letter or words in each plot denotes the variable.

Title Page

Abstract Introduction

Conclusions References

Tables Figures

◀ ▶

◀ ▶

Back Close

Full Screen / Esc

Printer-friendly Version

Interactive Discussion



A regional real-time forecast of marine boundary layers during VOCALS-Rex

S. Wang et al.

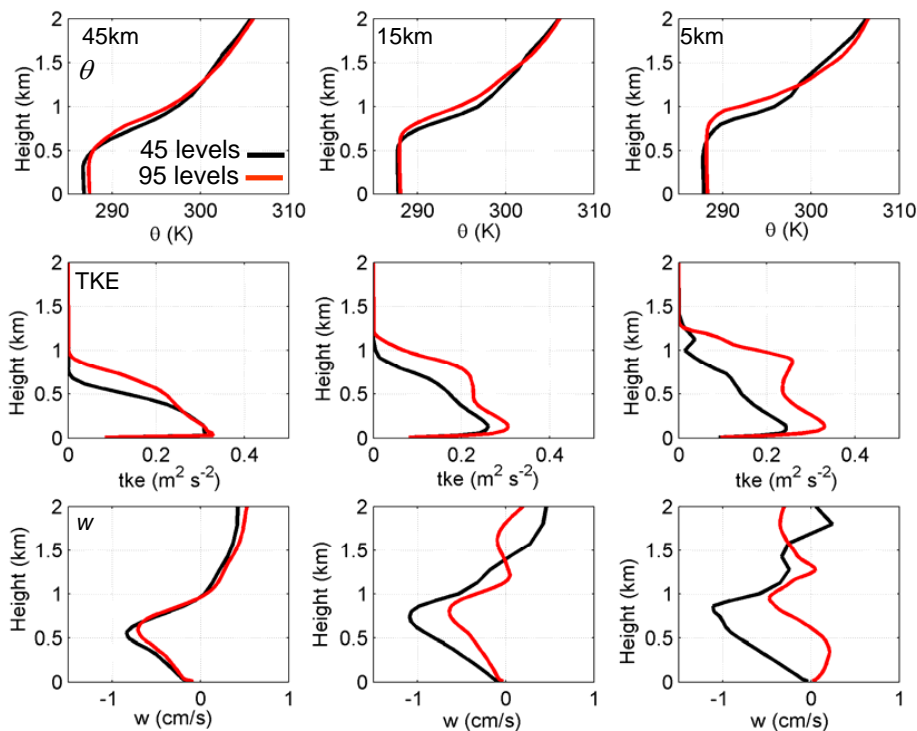


Fig. 17. Comparison of the time-averaged MBL profiles between the control (45 levels) and the high-vertical resolution (95 levels) simulation at 72° W and 20° S. Upper panels: θ ; and middle panels: TKE ; and the lower: w . The control forecast is denoted by black curves; and the high resolution by the red.

Title Page

Abstract

Introduction

Conclusions

References

Tables

Figures

◀

▶

◀

▶

Back

Close

Full Screen / Esc

Printer-friendly Version

Interactive Discussion